

Boundary mixing and nutrient fluxes in Mono Lake, California

Sally MacIntyre

Marine Science Institute and Institute for Computational Earth System Science, University of California, Santa Barbara, California 93106-6150

Kevin M. Flynn

Department of Geography, University of California, Santa Barbara, California 93106

*Robert Jellison and José R. Romero*¹

Marine Science Institute, University of California, Santa Barbara, California 93106-6150

Abstract

Temperature-gradient microstructure and nutrient profiling were undertaken at both an inshore and an offshore site on Mono Lake, California, to determine whether boundary mixing occurred and the effects on nutrient flux within the lake. Turbulence, as quantified by rates of dissipation of turbulent kinetic energy, was two to three orders of magnitude higher at the inshore site where the pycnocline intersected the bottom than at the same depths at an offshore station. The intense turbulence primarily occurred within 3.5 m of the sediment–water interface. In addition, temperature profiles were more incrementally stepped in the pycnocline inshore than offshore. The Turner angle indicated that double-diffusive processes may have augmented turbulent transport in the upper 10 m, where temperatures were inversely stratified, but not in the main pycnocline. Within the pycnocline, ϵ exceeded the threshold value for buoyancy flux ($\epsilon_{\text{thr}} = 15\nu N^2$) in 21% of the turbulent layers inshore but in only 1% of the layers offshore. The coefficient of vertical eddy diffusivity, K_z , was two to four orders of magnitude higher within 4 m of the bottom inshore than offshore at the same depths. Spatially averaged values of K_z , obtained from the heat-flux method using data obtained from both conductivity–temperature–depth (CTD) profiles and moored thermistor chains, were two orders of magnitude less than those obtained nearshore with microstructure profiling. From the differences in K_z , we inferred that most heat flux occurred due to boundary mixing at the base of the pycnocline inshore with the heat redistributed laterally by advection. Boundary mixing was initiated after winds were strong enough for the Lake number to decrease to a value of 2; thermocline compression and steepening of internal waves at the base of the pycnocline occurred, followed by packets of high-frequency internal waves critical for wave breaking. Calculated ammonium fluxes at the inshore site were sufficient to support daily rates of primary productivity in the deep chlorophyll maximum throughout the lake. These results indicate the vertical flux of nutrients across the nutricline in Mono Lake occurs over a limited area during intense mixing events initiated by high winds.

Whether mixing events occur as frequently throughout the pycnocline as they do near lateral boundaries has implications for heat and nutrient fluxes and spatial heterogeneity of ecological processes. The importance of mixing near boundaries was inferred by Munk (1966), who determined

¹ Present address: Centre for Water Research, University of Western Australia, Nedlands, WA 6009, Australia

Acknowledgments

We thank Darla Heil, Mike Emory, and Pete Kirchner for their help with fieldwork and chemical analysis and Manuela Lorenzi-Kayser for her assistance with data processing, programming, and graphics. Lorenz Moosmann contributed to the analysis. We thank the Centre for Water Research, University of Western Australia, for use of the software for microstructure analysis. The paper benefited from the constructive comments of John Melack, Craig Stevens, and two anonymous reviewers. We are especially grateful to Michael Head for his redesign and fabrication of the microstructure profilers and for his generous technical support.

Financial support was provided by National Science Foundation grants DEB93-17986 and DEB97-26932 to S.M. and DEB95-08733 to R.J. and J. M. Melack. K.M.F. received support from an NSF research training grant fellowship. Logistic support was provided by the Sierra Nevada Aquatic Research Laboratory, University of California Natural Reserve System.

that large mixing rates were needed at lateral boundaries to account for the observed distributions of temperature and salt in the abyssal ocean. Recent observations and more complex models support Munk's inference (Garrett 1991; Toole et al. 1994; Ledwell and Hickey 1995; Lueck and Mudge 1997). Processes causing mixing at lateral boundaries include internal waves shoaling at the sediment–water interface, shear from the upward and downward movement of the pycnocline, geometric focusing of internal waves, and flow over topographic features (Ericksen 1982, 1985, 1998; Thorpe 1987, 1995; Taylor 1993; Imberger 1994; Ivey et al. 1995; Maas and Lam 1995). Enhanced mixing has also been observed in deep basins when the topography is rough (Polzin et al. 1997). If these processes that lead to vertical mixing are coupled with horizontal advection, the fluxes will appear to have occurred throughout the basin.

Oceanic measurements of increases in energy dissipation rates over sloping boundaries include Lueck and Mudge's (1997) finding increases of up to four orders of magnitude between dissipation rates in the interior and those above the sloping sides of Cobb Seamount (46°45'N, 130°50'W). Toole et al. (1994) reported an increase of up to one order of magnitude above Fieberling Guyot (32.5°N, 127.7°W). Van Haren et al. (1994) found an increase of one order of

magnitude in dissipation rates in the benthic boundary layer of the Scotian Shelf off Nova Scotia.

In lakes, the observed effects have been either indirect or muted. In 4.8 km² Lake Alpnach, Gloor et al. (1994) documented sediment concentrations two to four times higher within the benthic boundary layer than in the overlying water. They hypothesized that increased concentrations were due to increased shear associated with burstlike increases in current velocity. The velocity increases were found in near-shore regions with sloping boundaries. Wiegand and Chamberlain (1987), working in 9.5 km² Wood Lake, found wave-induced bottom currents to be too low for resuspension. Lemmin (1987), in an analysis of internal waves in a moderately sized basin, concluded that in lakes with low to moderate wind speeds, boundary mixing would not be an important process. However, Wüest et al. (1996) found dissipation rates to increase from 10⁻⁹ to 4 × 10⁻⁸ m² s⁻³ from the interior to the benthic boundary layer of Lake Alpnach. However, based on the rapid decreases in potential energy of the internal wave field following strong wind forcing, energy dissipation rates of 10⁻⁶ m² s⁻³ were predicted due to boundary mixing in a large lake (Saggio and Imberger 1998).

The effects of boundary mixing are not necessarily limited to the boundary layer adjacent to the bottom. As the internal wave field interacts with a sloping bottom, the internal wave spectrum is altered (Eriksen 1982, 1985; Siedler and Paul 1991). The increase in energy, shear, and strain may be due to wave reflection (Gregg and Kunze 1991). Depending on bottom slope, the increased wave strain may lead to instabilities in the density profile that can collapse and mix (Eriksen 1998). For example, enhanced mixing occurred several hundred meters above Cobb Seamount and Fieberling Guyot (Lueck and Mudge 1997; Toole et al. 1997). The enhanced mixing extended laterally up to 10 km away from Cobb Seamount. Instabilities can also arise in the lee waves formed as flow passes topographic features (Thorpe 1984). For instance, the coefficient of eddy diffusivity was elevated for at least 1,000 m above the rough topography in the Brazil Basin (Polzin et al. 1997). The overall effect of boundary mixing on heat and nutrient fluxes will depend on the vertical and horizontal extent of enhanced mixing.

We present direct evidence for enhanced mixing near lateral boundaries, which we call "boundary mixing," in Mono Lake, a moderately sized (160 km²) temperate lake. We also provide the first estimates of nutrient fluxes due to this mixing. Rates of turbulent kinetic energy dissipation and coefficients of eddy diffusivity are calculated from temperature-gradient microstructure profiles taken at inshore and offshore stations. The inshore station was selected so the pycnocline would intersect a sloping bottom; the offshore site was 2 km distant with bottom slopes of 0.1%. To determine the relative importance of boundary mixing to mixing in the pelagic zone, K_z values obtained from the microstructure profiles were compared to ones calculated from heat fluxes using lake-wide CTD profiles and thermistor chain data. Time-series data from moored thermistor strings are used to determine the basin scale modes and to describe the sequence of events prior to and during the period of intense mixing. We assess the spatial extent of boundary mixing, compute the

resulting nutrient fluxes, and address the implications of these fluxes for primary productivity within deep chlorophyll maxima.

Study site—Mono Lake (Fig. 1) is a saline lake located in the Great Basin at the eastern base of the Sierra Nevada (119°W) at a latitude within the prevailing westerlies (38°N). Except on its northwestern shore, where it abuts the mountains, the basin immediately surrounding the lake consists of low-gradient slopes (~1°, Mason 1967). The predominant wind pattern over the lake through much of the year consists of strong diurnal winds from the SSW. Daily average wind speeds of 6–8 m s⁻¹ are common during the summer mid-lake. Winter storms, with more persistent, higher winds, are associated with the passage of frontal systems. The northwestern embayment is usually the last area to experience diurnal winds and often remains protected throughout the day. Occasionally, meteorological conditions result in high winds directly over the mountain ridges, with subsequent strong downdrafts to which the northwestern embayment is susceptible. Winds from other quadrants associated with cyclonic flows generally spread across the entire lake. Two relatively large islands, Negit and Paoha with peaks rising about 40 and 100 m above the lake surface, respectively, result in sheltered lee areas and associated bending of the wind field depending on its direction.

Mono Lake's bathymetry slopes steeply along the SW shore and along the southern and eastern sides of Paoha Island (Pelagos Corp. unpubl. data), with slopes ranging from 10 to <1%. Our inshore site, S10, was located where bottom slopes were 4%. This site is in the lee of a promontory for cyclonically traveling disturbances; there, bottom slopes were 10% (Figs. 1, 2). Our offshore site, S30, was located at 38-m depth in the deepest, large basin of the lake where the bottom was essentially flat (slope = ~0.1%). The thermistor chain was located at the base of a promontory 1 km east of S10 where bottom slopes were 3%.

Freshwater inputs near our study sites include Lee Vining Creek, whose mouth is at the promontory inshore of Sta. 9, and Rush Creek, whose mouth is at the promontory to the west of S10. The lake has no outlets. The biological, chemical, and physical responses of Mono Lake to changes in hydrological inputs, including seasonal and yearly estimates of K_z and ammonium fluxes, are presented in Jellison and Melack (1993a,b), Jellison et al. (1993), Romero and Melack (1996), and Romero et al. (1998). The plankton community of Mono Lake has few species. Nonmotile coccoid chlorophytes, coccoid cyanobacteria, and several bacillariophytes dominate the phytoplankton, while the brine shrimp, *Artemia monica*, is the only macrozooplankton. Phytoplankton are nitrogen limited (Jellison 1993).

Due to increased freshwater inputs in 1995, the density difference across the pycnocline became large enough that the combined effects of wind mixing and autumn cooling were insufficient for the lake to mix in its entirety. The resulting meromixis limits the flux of nutrients to the euphotic zone. Mixing near sloping boundaries or topographic features may be critical for nutrient flux to the euphotic zone.

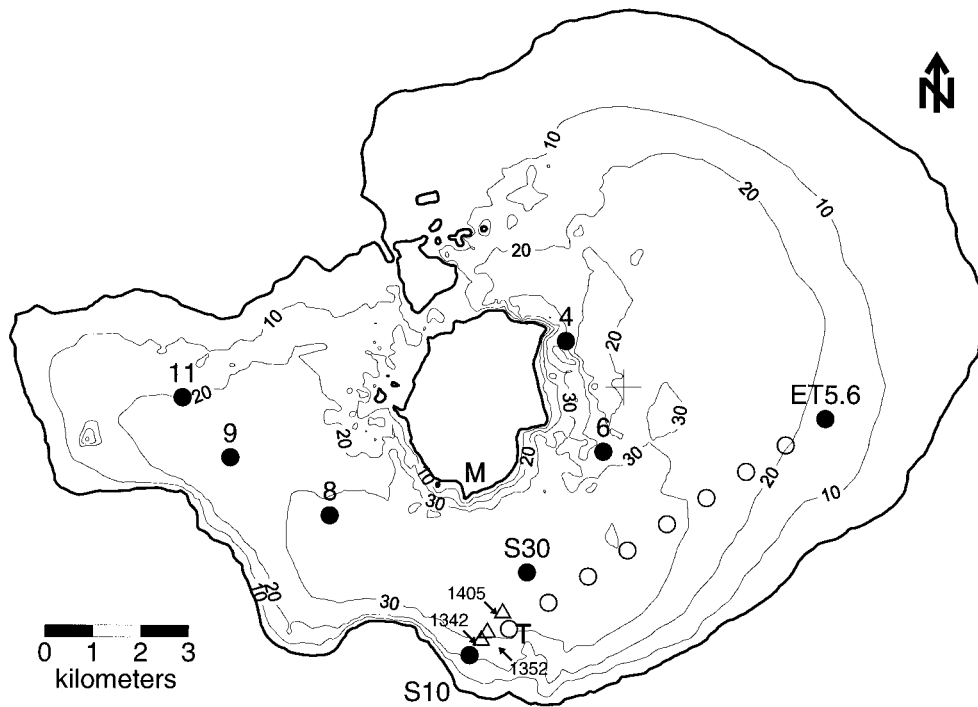


Fig. 1. Bathymetric map of Mono Lake with sampling stations. Contour intervals are in meters. The locations of the meteorological station and thermistor chain are marked with an *M* and a *T*, respectively; the numbers correspond to sampling stations. S10 and S30 were the inshore and offshore sites for microstructure profiling. The open circles mark the CTD transect stations between S10 and ET5.6. CTD profiles on 20 September were obtained at all numbered stations; on 14 October, at all numbered stations, along the transect line, and at four additional sites. Triangles mark locations of microstructure transect; times of sampling in hours are noted.

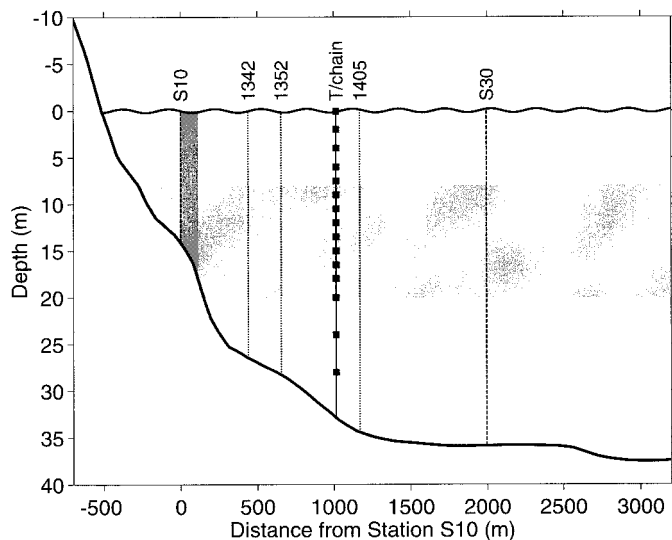


Fig. 2. Sampling locations relative to bottom bathymetry. S10 and S30 are locations of inshore and offshore microstructure profiling; locations of microstructure profiles on the transect are indicated by their times in hours (1342, 1352, and 1405 h); depths of WaDaRs are indicated by closed boxes. Note that the thermistor chain (T/chain) is to the east of the transect line (Fig. 1). The gray band around S10 indicates the full range of sampling locations. The gray, horizontal band indicates the pycnocline.

Methods

Meteorological and radiation measurements—Wind speed and direction (R. M. Young model 05305 wind monitor AQ), relative humidity and air temperature (Vaisala model HMP35C and Omnidata model ES-060 thermistor), rainfall (Qualimetrics tipping bucket rain gauge), and photosynthetically available radiation (PAR; Li-Cor model LI-190S) were measured at the southern shore of Paoha Island in Mono Lake (Fig. 1). A Campbell Scientific data logger (model CR10) sampled each sensor every second, and data were stored as 10-min averages. Peak values of the wind speed and vector-averaged wind velocity were among the data recorded in each 10-min period.

Additional measurements of short-wave radiation (285–2,800 nm), long-wave radiation (3,000–50,000 nm), and PAR were obtained 7 km from the lakeshore at Cain Ranch. A Campbell Scientific data logger (model CR10) sampled each sensor every 10 s, and the data were stored as 1-h averages.

Attenuation of PAR within the water column was measured with a submersible Li-Cor sensor (model LI-192S sensor, model LI-185 meter) at 0.5-m intervals.

Microstructure profiling—Table 1 summarizes all instrument deployments, and Fig. 2 indicates locations of microstructure profiling and the thermistor chain relative to bottom

Table 1. Schedule of instrument deployments and nutrient and chlorophyll sampling.

Measurement	Dates	Location	Time (h), (n,* †)
CTD	20 Sep	Buoyed stations	
	14 Oct	Buoyed stations and 12 others	
CTD transects	11 and 12 Oct	ET5.6 to S10	~0700–0930 h
Thermistor chain	10 Oct–25 Oct	1 km from S10	
Microstructure	11 Oct	S10 (inshore)	1142–1328 h (5u)
	12 Oct		1414–1537 h (8u)
			1558–1617 h (2d)
	13 Oct.		1145–1331 h (5d)
			1535–1556 h (3d)
Microstructure	11 Oct.	S30 (offshore)	1511–1549 h (5u)
	12 Oct.		1157–1340 h (5u)
	13 Oct.		1418–1427 h (2d)
Microstructure	13 Oct.	Transect between S10 and S30 (Fig. 1)	1342 h (1, d)
			1352 h (1, d)
			1405 h (1, d)
NH ₄ and Chl <i>a</i>	11 Oct.	S10 (inshore)	0955, 1410 h
	12 Oct.		0925, 1510 h
	13 Oct.		1600 h
	14 Oct.		0915 h
NH ₄ and Chl <i>a</i>	11 Oct.	S30 (offshore)	0720, 1620 h
	12 Oct.		0745, 1310 h
	13 Oct.		1445 h
	14 Oct.		1235 h

* Number of microstructure profiles.

† Up (u) or down (d) microstructure cast. Upward profiles begin sampling within 1 m of the bottom and continue to the surface; downward profiles begin sampling 0.65 m below the surface and continue to within ~10 cm of the bottom.

bathymetry and depth of the thermocline. Temperature, temperature gradients, conductivity, and pressure were measured at a frequency of 100 Hz using temperature-gradient microstructure profilers (self-contained autonomous microstructure profiler or SCAMP, Precision Measurement Engineering) based on a modification of the design of Carter and Imberger (1986). The SCAMPs are ca. 0.7 m in length. Deployed in either rising or falling mode, they move at a speed of ca. 0.1 m s^{-1} ; with a 100-Hz sampling rate, their spatial resolution is 1 mm. Data are transmitted up an umbilical to a laptop computer. The sensors included two fast-response thermistors (FP07, time constant = ~10 ms) separated by ca. 1 mm, with one paired with a microconductivity electrode (time constant = ~4 ms), which failed. A slower but more stable thermistor-conductivity sensor pair was located ca. 3 cm below the fast-response sensors. The thermistor had a time constant of 450 ms; the conductivity sensor had a spatial resolution of ca. 1 cm. The depth transducer is ca. 0.65 m below the FP07 thermistors. Data from the fast-response sensors were sharpened and smoothed digitally (Fozdar et al. 1985) before computing conductivity normalized to 25°C, density, and rates of energy dissipation. The instrument was calibrated before and after sampling.

Lake-wide and time-series measurements of temperature and conductivity—A SeaBird CTD (Sea-Bird Electronics model Seacat SBE 19) was used to profile temperature and conductivity at several sampling stations around the basin and along a transect from S10 to ET5.6 (Fig. 1). Its buoyancy was adjusted to ensure sampling ca. eight times per meter in free-fall descent. The CTD is calibrated annually

by Sea-Bird Electronics. The data from the thermistor and conductivity cell were offset by 750–900 ms to reduce spiking resulting from the slower response time of the thermistor. Time-series data of temperatures at 15 depths were obtained with self-contained temperature loggers (WaDaRs, TSKA) deployed on a subsurface mooring near Sta. S10 (Figs. 1, 2). Each WaDaR has an accuracy of 0.01°C , a resolution of 1.4 mdeg, and a time constant of ~1–3 min. For the faster time constant, the spectral rolloff would begin at 1,000 cpd (cycles per day); for the slower, it would begin at 480 cpd. The units were calibrated before and after deployment against a platinum resistance thermometer with an accuracy of 0.6 mdeg.

Chemical analysis—Ammonium ($\text{NH}_4^+ + \text{NH}_3$) concentrations were measured by the indophenol-blue method (Strickland and Parsons 1972). Chlorophyll *a* (Chl *a*) was determined by spectrophotometric analysis with correction for phaeopigments (Golterman 1969). Details for both procedures are given in Jellison et al. (1993).

Calculations—Density was calculated from temperature and conductivity corrected to 25°C using an equation of state developed for Mono Lake (Jellison et al. in press). Density profiles from the SCAMP were calculated using data from an FP07 thermistor and the larger conductivity sensor. The FP07 thermistor was filtered to match the time constant of the larger conductivity sensor (180 ms) and offset by 0.4 s, so values from both sensors were from the same location.

For the CTD profiles, density was computed after averaging the conductivity profiles over 1-m intervals centered

on every meter; corresponding temperatures at each meter were obtained from interpolated temperature profiles.

Rates of energy dissipation, ϵ , were computed by a least-squares fit of the power spectral densities of the temperature-gradient signal to the Batchelor spectrum (Dillon and Caldwell 1980; Imberger and Ivey 1991). Power spectral densities were calculated in segments in which the turbulence was determined to be statistically stationary (Imberger and Ivey 1991). Two problems arose with this approach. Different values of the threshold for the distance function (Imberger and Ivey) were required for the upper mixed layer and for the thermocline, and segments were often several meters in extent. To overcome these problems, we developed an interactive procedure for segmenting that relies on the fact that the distance function essentially separates depth intervals with different frequencies of fluctuations in the temperature-gradient signal. First, we segmented using a threshold value that reasonably separated segments with different characteristics. Then, we inspected each segment, further subdividing it if distinct regions of high and low frequency remained. We also subdivided segments to be <1 m in vertical dimension. Values of vertical eddy diffusivity, K_z , were calculated using Osborn's (1980) model, $K_z = \Gamma \epsilon N^{-2}$, where Γ is the mixing efficiency, and N is the buoyancy frequency. We let $\Gamma = 0.25$, the upper limit in Ivey and Imberger's (1991) analysis and similar to the mean mixing efficiency of 0.265 found by Oakey (1985). Γ increases with increasing $\epsilon/(vN^2)$, where v is kinematic viscosity. Ivey and Imberger (1991) found Γ equivalent to 0.25 for $\epsilon/(vN^2) \approx 15$; Ruddick et al. (1997) found its mean value to range from 0.1 to 0.25 as $\epsilon/(vN^2)$ goes from 30 to 500. By using $\Gamma = 0.25$, we are calculating the upper limit of K_z . The buoyancy frequency $N = (-g/\rho \partial\rho/\partial z)^{1/2}$, where ρ is density, g is gravity, and z is depth. We assumed the coefficient of eddy conductivity was equal to that of eddy diffusivity and calculated the flux of ammonium as $F = K_z \partial[\text{NH}_4^+]/\partial z$.

Arithmetic averages of ϵ were determined for 1-m intervals by determining the percentage of the interval occupied by a segment, multiplying that percentage by ϵ , summing the contributions from each segment, and assuming that ϵ equaled $10^{-10} \text{ m}^2 \text{ s}^{-3}$ in the portion of the interval without segments. These depth-averaged values of ϵ were then averaged for all profiles. Because turbulence occurs intermittently, and because samples of ϵ are often approximately lognormal, we also computed the maximum likelihood estimator X_{mle} for ϵ and for K_z (Baker and Gibson 1987). $X_{\text{mle}} = \exp(m + s^2/2)$, where m and s^2 are the arithmetic mean and sample variance of $\ln(\epsilon)$ or of $\ln(K_z)$. Both m and s^2 were obtained using 100 bootstrap samples. Only segments with Batchelor spectra were included. Confidence intervals were computed from the percentile bootstrap where the 2.5 and 97.5 percentile values are used as the limits for the 95% confidence interval (Dixon 1993).

Values of K_z were calculated from the thermistor chain data and CTD profiles with the heat-flux method (Jassby and Powell 1975), using the lake-wide CTD profiles obtained on 20 September and 14 October 1995 and the thermistor chain data from 11 to 25 October (Fig. 1). Adaptations of the method to improve reliability are provided in Jellison and Melack (1993b). CTD casts were obtained at eight stations

on 20 September and at 20 stations on 14 October and averaged to remove effects of spatial variability and differences in isopycnal depths due to internal wave motion. To avoid bias from internal waves with the moored thermistor chain data, heat contents were computed by averaging over 3-d periods: 11–13 October, 17–19 October, and 22–24 October. The change in heat content was computed over the 5- and 6-d intervals. Data from the heat-flux method are only valid where the lake is gaining heat; during these averaging periods, heat was being gained below 10.5 m. Consequently, results were calculated for depths of 12 m and below. Hypsographic data derived from detailed bathymetry (Pelagos Corp. unpubl. data) were used to compute heat content and fluxes within different volumes of the lake.

Isotherm depths were determined using linear interpolation between the depths of the WaDaRs. Power spectra of isotherm displacements were computed using 3.8-d intervals (16,384 samples collected every 20 s), beginning at 1800 h on 10 October and every 6 h thereafter. The spectra were computed using a Hanning window and linear detrending. Eighty percent confidence intervals were computed. Power spectral densities were multiplied by the mean buoyancy frequency at depth so that the results would be proportional to energy.

Coherence spectra were found for a 7.6-d (32,768 samples) window beginning at 0 h on 11 October. The spectra were computed using 75% overlapping windows of 16,384 samples each. Linear detrending and a Hanning window were applied to each window before computing the periodogram. Uncertainty estimates were computed using the procedure outlined in Bendat and Piersol (1986). Phase shifts were obtained by computing the transfer function using the same windowing procedure.

The Wedderburn number, $W = g'h_1^2/(u_*^2L)$, and the Lake number, $L_N = gS_i(1 - (z_i/H))/(\rho u_*^2 A^{1.5}(1 - z_g/H))$ were calculated as in Imberger and Patterson (1990); both are ratios of the density stratification to the wind forcing but L_N better represents a lake's complex stratification and bathymetry. Reduced gravity g' is equal to $g\Delta\rho/\rho_o$, where $\Delta\rho$ is the density difference across the pycnocline, ρ_o is mean density, g is gravity, h_1 is the depth from the surface to the depth of the plane on which the first vertical mode internal wave tilts, u_* is the friction velocity in water computed as $u_* = (\rho_a/\rho_w C_d U^2)^{1/2}$, where C_d is the drag coefficient modified for winds measured at ~ 3 -m height above the water surface, L is the length of the lake, z_i is the height to the center of the metalimnion, z_g is the height to the center of volume of the lake, A is lake area, H is the depth of the lake, and S_i is the overall stability of the lake. The overall stability is the energy required to mix the entire water column against the potential energy due to its stratification and is given by $S_i = \int_0^{z_m} (z - z_g)A(z)\rho(z)dz$, and z_m is maximum depth of the lake. We used a drag coefficient at 10 m of 1.3×10^{-3} and adjusted it to the height of the anemometer using the law of wall scaling.

The Turner angle, used to determine if double-diffusive processes are occurring, is the arctangent of $(N_T^2 - N_S^2)/(N_T^2 + N_S^2)$, where $N_T^2 = g\alpha dt/dz$ and $N_S^2 = g\beta dS/dt$, and the signs are chosen so that positive N_T^2 and N_S^2 correspond to stable

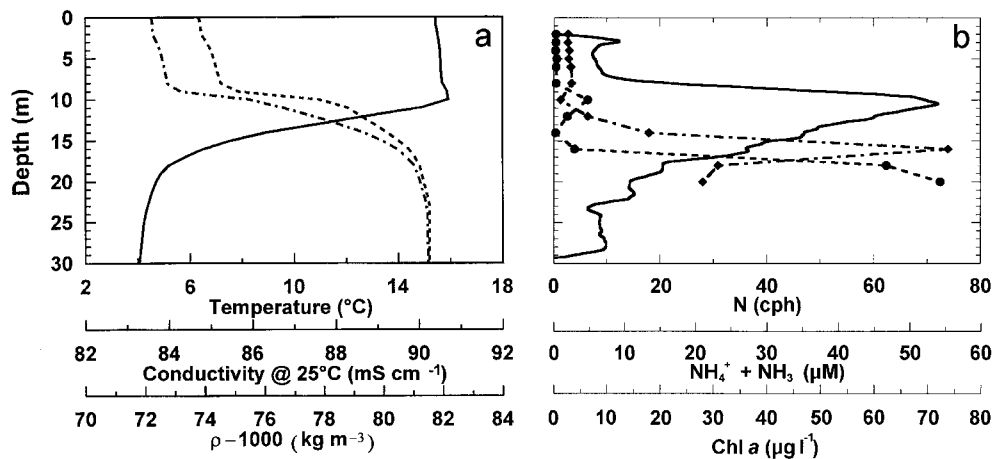


Fig. 3. (a) Profiles of temperature (-), conductivity (- -), and density (-·-) in Mono Lake on 11 October 1995 using lateral averaging of profiles on the transect between S10 and ET5.6 and the profile at S30. Profiles were taken between 0732 and 0944 h. (b) Profiles of ammonium plus ammonia (•), Chl *a* (◆), and buoyancy frequency *N* (-) on 11 October 1995 at S30. Nutrient data were collected at 0720 h. *N* profile is based on the CTD profile taken at S30.

T and *S* stratification (Ruddick 1983). Values of α and β were obtained from Romero et al. (1998).

Results

Stratification and meteorology—Temperature, conductivity, and density had features in common at both S30 and S10 over the course of the experiment. Temperatures tended to be inversely stratified in the upper 10 m, with a temperature maximum between 8- and 11-m depth; a pronounced thermocline extended from this maximum to 18-m depth (Fig. 3a). The top of the chemocline began at ~8 m, offsetting the inverse temperature gradient such that the top of the pycnocline was stably stratified. Due to the combined thermal and chemical stability, the density difference across the pycnocline was 9 kg m⁻³. The buoyancy frequency *N* indicates that the water column was stably stratified throughout, with a maximum at 10 m of 70 cycles per hour (cph) (0.12 s⁻¹) (Fig. 3b). At the base of the pycnocline, 18 m, *N* = 20 cph. The values of *N* in both the mixolimnion (surface to 8-m depth) and below the pycnocline were comparable to moderately stratified oceanic waters and could sustain internal waves.

Ammonium and chlorophyll profiles show the nutricline beginning at 15-m depth with the chlorophyll maximum above it (Fig. 3b). NH₄⁺ concentrations were <1 μM in the upper 8 m, increased to 5 μM at 10-m depth, again <1 μM at 14-m depth, and increased below that depth, reaching a maximum of 55 μM at 20 m. The concentration of Chl *a* was 3 μg liter⁻¹ in the upper 8 m, decreased slightly at 10 m where NH₄⁺ concentrations increased, and increased below that depth, reaching a maximum of 73 μg liter⁻¹ at 15-m depth.

The depth of the oxycline varied; on 11 October, it occurred between 5 and 12 m. By 12 October, it was sharper; concentrations were 7 mg liter⁻¹ at 10 m with anoxia (O₂ concentration ≤ 0.5 mg liter⁻¹) by 14-m depth. On 13 Oc-

tober, the oxycline extended from 10 to 15 m, with concentrations of 5 mg liter⁻¹ at 10 m and anoxia at 15 m.

Solar insolation was similar for 11–13 October because of the lack of appreciable cloud cover (data not shown). Daily maxima of surface PAR was 1,500 μE m⁻² s⁻¹. Air temperatures slightly lagged the maxima in irradiance, with daily maxima up to 23°C. Relative humidity was out of phase with air temperatures, with daytime minima of 25% and nighttime maxima of 80%. The depth of the euphotic zone, given as the depth where PAR is 1% of surface values, was 14 m.

Wind forcing and isotherm displacements—The highest and most persistent winds occurred at the start of our field experiment (Fig. 4). On 11 October, winds were from the SSW, averaged 10 m s⁻¹ with gusts of 15 m s⁻¹, and persisted for ca. 7 h. For a short interval after midnight, winds averaged 13 m s⁻¹. On 12 October, winds were from the NE and averaged 8 m s⁻¹, with gusts up to 11 m s⁻¹ for a 7-h period. Winds dropped to 4 m s⁻¹ the night of 12 October. For the rest of the 2-week period, average winds only exceeded 7 m s⁻¹ twice and for shorter intervals.

The largest amplitude isotherm displacements occurred in response to the strong wind forcing on 11 and 12 October and again on 21 October. As a result of the wind forcing on 11 October, the thermocline tilted, causing isotherm displacements with amplitudes up to 1 m. The thermocline remained tilted until the wind dropped and then tilted again as the wind increased from 6 to 7 m s⁻¹. The strong wind forcing of 11 October combined with the effects of previous forcing led to a complex internal wave field, with some of the isotherm displacements in phase, others not. The largest amplitude displacements occurred at the base of the pycnocline. By 15 October, the amplitude of the isotherm displacements was muted relative to the earlier period, suggesting internal wave activity had dampened.

Microstructure profiles—Microstructure profiles were obtained during the windy period on 11 October, at the onset

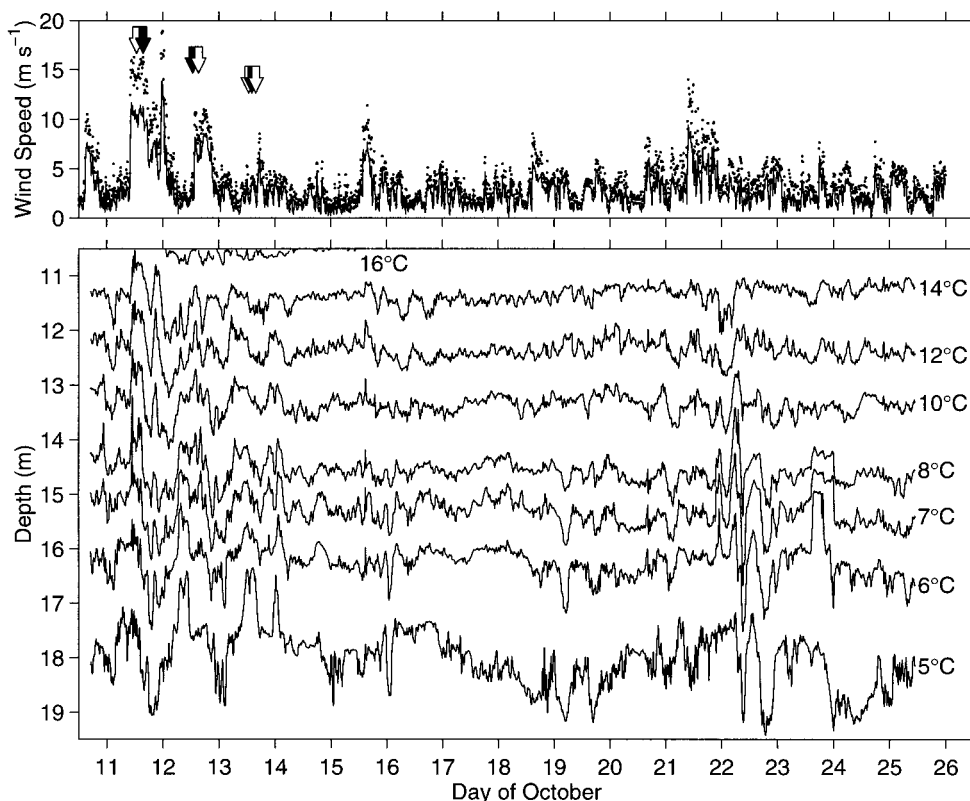


Fig. 4. Ten-minute average wind speeds (upper panel) and isotherm displacements within the pycnocline (lower panel) from 1800 h on 10 October through 1200 h on 25 October 1995. Tic marks indicate midnight. Isotherm temperatures are indicated in figure. Arrows in upper panel indicate times of microstructure sampling; clear arrows indicate S10. Dots indicate maximum gusts during each 10-min period.

of and during the windy period on 12 October, and during the moderate to low winds on 13 October (Fig. 4; Table 1). Profiles were taken at an inshore station (S10) and at an offshore station (S30) to determine whether the intensity of turbulence differed when sampling at depths where the pycnocline intersected a sloping boundary (Fig. 2).

While the temperature profiles at both stations showed a temperature maximum between 8- and 10-m depth and decreasing temperatures below that feature, the profiles in the upper waters varied with diurnal heating and movements of freshwater inputs (Figs. 5, 6). The variations in temperature and salinity above the pycnocline will not be addressed in this paper.

Within the pycnocline on 11 October, temperature profiles were more steplike inshore than offshore; a thermal inversion indicative of an overturning event occurred inshore at 1222 h.

Profiles of energy dissipation rates from the two stations had several features in common on the first sampling day (Figs. 5, 6). The largest values of the rate of energy dissipation occurred in the upper 10 m, with values of $10^{-5} \text{ m}^2 \text{ s}^{-3}$ near the surface due to wind inputs. In some profiles, ϵ reached $3 \times 10^{-5} \text{ m}^2 \text{ s}^{-3}$. These values are among the highest measured in surface waters of lakes or oceans (Anis and Moun 1994, 1995) and may be associated with breaking waves. Values of ϵ decreased below the surface, rising again

in association with variations in thermal structure and with the layer of warm water. For instance, the steplike increase in temperature at 4 m at 1151 h (S10) had elevated values of ϵ immediately above it, suggesting a layer of high shear. While the upper 10 m tended to be turbulent throughout, below 10 m, the turbulence was patchy and discontinuous, with $\epsilon < 10^{-7} \text{ m}^2 \text{ s}^{-3}$. Below 13-m depth, ϵ was $< 10^{-8} \text{ m}^2 \text{ s}^{-3}$, with exceptions occurring at 1222 h in the inversion at 12.5 m and at the bottom of the profile.

On 12 October, temperatures within the thermocline decreased smoothly offshore, with the only inversion at 18 m. Inshore, temperature profiles below the warm layer were stepped, with 8 of the 10 profiles showing inversions within 3 m of the bottom of the profile. The inversions were up to 0.5 m in vertical extent.

Rates of energy dissipation differed markedly within the thermocline at inshore and offshore sites on 12 October. At both locations, high values tended to occur in the temperature inversion at the top of the thermocline. However, offshore, ϵ was $< 3 \times 10^{-8} \text{ m}^2 \text{ s}^{-3}$. In contrast, ϵ frequently exceeded $10^{-7} \text{ m}^2 \text{ s}^{-3}$ inshore where temperature profiles were stepped. In 8 of the 10 profiles, ϵ reached $10^{-6} \text{ m}^2 \text{ s}^{-3}$. Elevated values of ϵ occurred intermittently throughout the thermocline; however, in all 10 of the microstructure profiles taken that day, high values of ϵ occurred within 3.5 m of the bottom. No such increases occurred offshore.

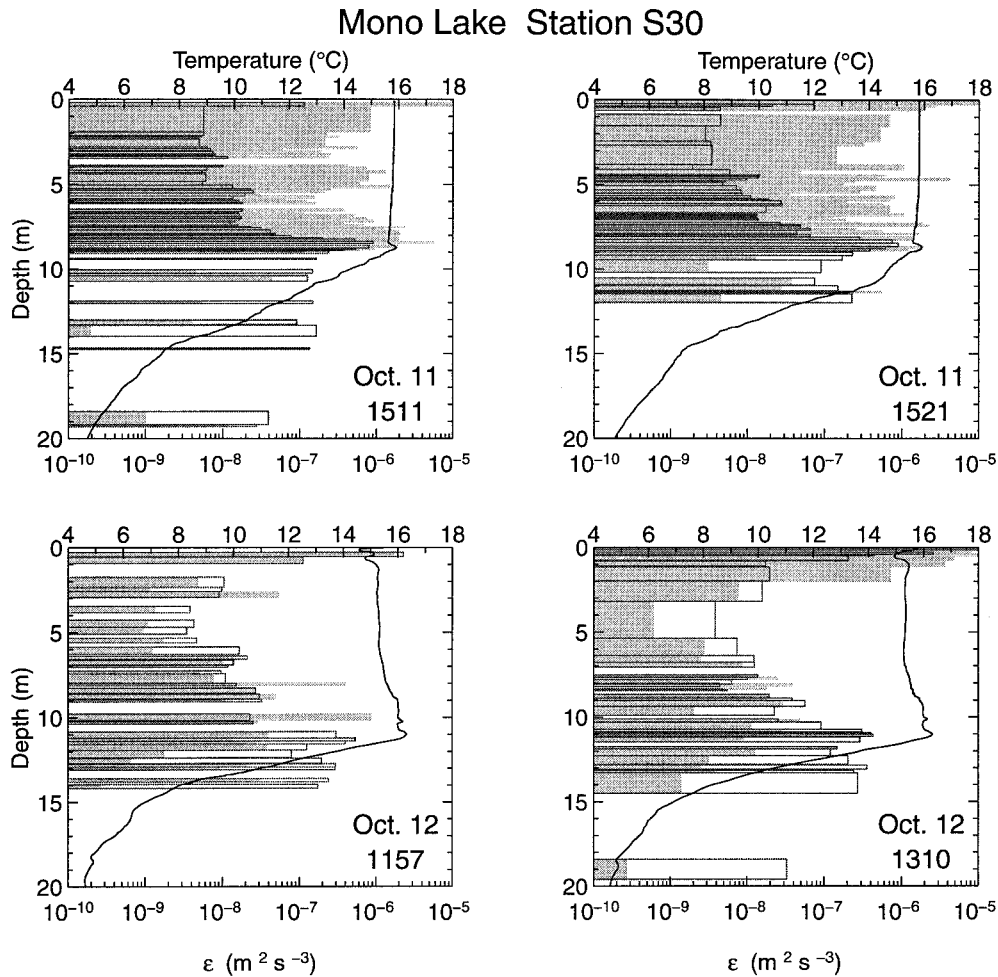


Fig. 5. Representative profiles of temperature (—), rate of dissipation of turbulent kinetic energy (filled areas), and ϵ_{thr} (open bars) at S30 at 1511 and 1521 h on 11 October and 1157 and 1310 h on 12 October. Data are only plotted for segments whose spectra fit a Batchelor spectrum. Only the upper 20 m are illustrated.

Within the thermocline, temperature profiles on 13 October had the same pattern as those on 12 October, with smooth profiles below the temperature maximum offshore and stepped ones inshore. Offshore, ϵ was $<10^{-8} \text{ m}^2 \text{ s}^{-3}$ below the warm layer; inshore values were again typically above $10^{-7} \text{ m}^2 \text{ s}^{-3}$ and often equal to $10^{-6} \text{ m}^2 \text{ s}^{-3}$ (MacIntyre 1998). The largest enhancement was often, but not always, in the bottom meter. Values reached $8 \times 10^{-6} \text{ m}^2 \text{ s}^{-3}$ at one site inshore of S10.

Averaged profiles for the 3 d further corroborate the pattern seen in individual profiles (Fig. 7). Arithmetic averages of ϵ and X_{mle} , the maximum likelihood estimator of ϵ , were similar at the inshore and offshore stations on 11 October. Highest values occurred near the surface, decreased in the interior of the upper mixed layer, peaked at 8.5 m, and steadily dropped below that. One profile from S10 had an elevated value of ϵ below 10 m. Data from the offshore site on 12 October repeated the pattern established on 11 October. Values of ϵ dropped from their peak of $10^{-7} \text{ m}^2 \text{ s}^{-3}$ at 10 m to $<10^{-9} \text{ m}^2 \text{ s}^{-3}$ below 14.5-m depth. Values of $10^{-10} \text{ m}^2 \text{ s}^{-3}$ are at the threshold of the instrument and indicate

minimal turbulence or that a Batchelor spectrum was not observed. Inshore, ϵ initially decreased below the peak at 10.5 m, but values increased and were indicative of moderate turbulence between 13.5 and 16.5 m. At 14.5-m depth, ϵ was three orders of magnitude higher than offshore. The pattern repeated itself on 13 October, with ϵ inshore one to two orders of magnitude higher than offshore. The low value at 16.5 m inshore resulted because the bottom meter was not turbulent in the two profiles that extended beyond 16 m.

Coefficients of vertical eddy diffusivity—Maximum likelihood estimates of K_z corroborate the enhanced mixing inshore between 12.5- and 15.5-m depths (Fig. 8). K_z values were comparable inshore and offshore in the upper 10 m, but they were two to four orders of magnitude higher inshore than offshore between 12.5- and 15.5-m depths. Below 12.5-m depth, K_z values offshore were less than or equal to the coefficient of molecular conductivity ($\sim 10^{-7} \text{ m}^2 \text{ s}^{-1}$). As mentioned previously, assuming $\Gamma = 0.25$ implies these estimates of K_z are an upper limit.

K_z values calculated from the time series of temperature

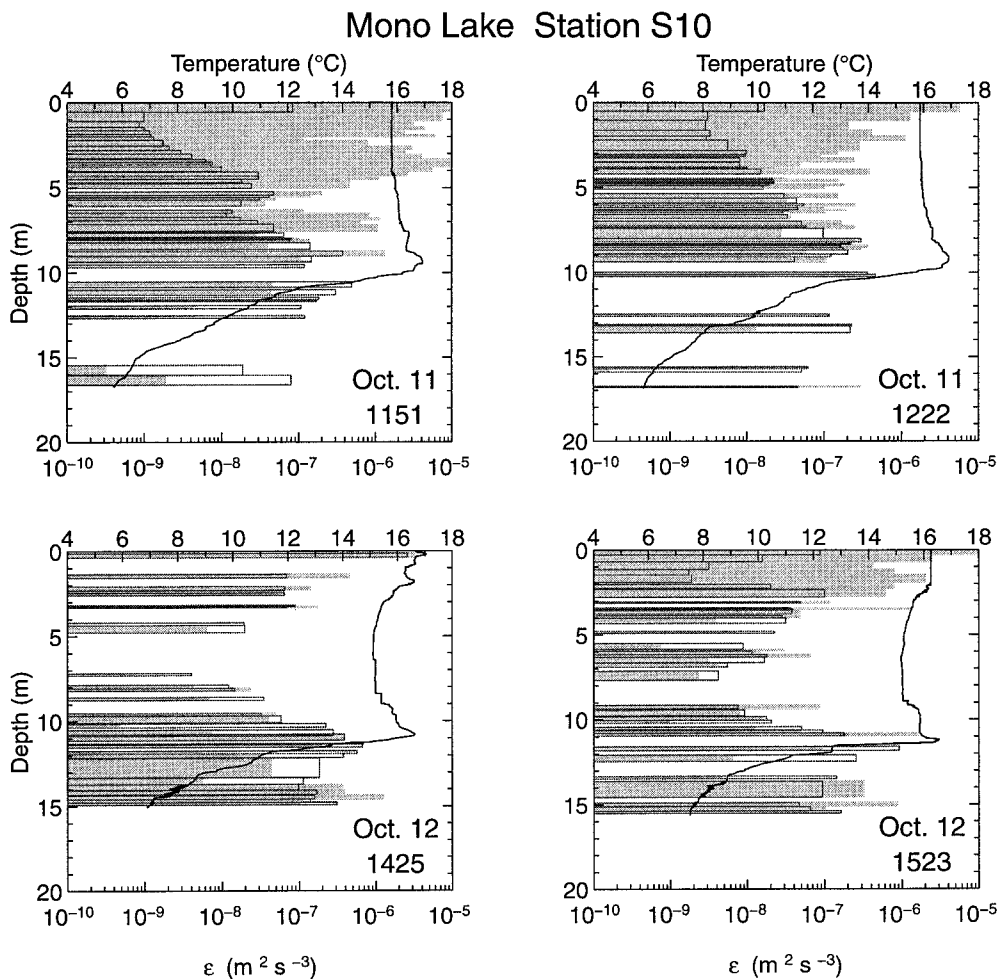


Fig. 6. As for Fig. 5 but for inshore station (S10). Upper panels, 1151 and 1222 h on 11 October; lower panels, 1425 and 1523 h on 12 October 1995.

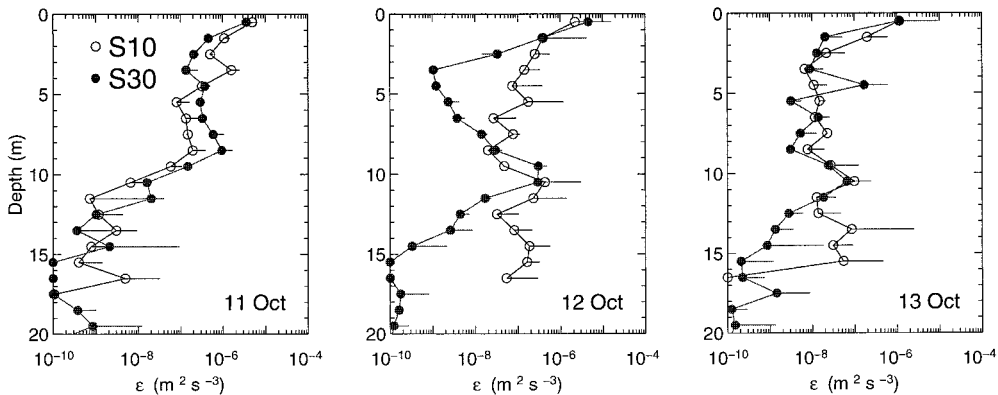


Fig. 7. Profiles of arithmetic average and maximum likelihood estimator of rates of energy dissipation (ϵ) on 11 October, 12 October, and 13 October at inshore (S10, \circ) and offshore stations (S30, \bullet). Numbers of profiles: 5, 10, and 8 at S10 and 5, 5, and 5 at S30 on the respective 3 d. Data from the offshore transect on 13 October are averaged with the data from S30. Arithmetic averages are indicated by \circ and \bullet ; maximum likelihood estimator as end of horizontal line. Locations with no turbulence are indicated with $\epsilon = 10^{-10} \text{ m}^2 \text{ s}^{-3}$.

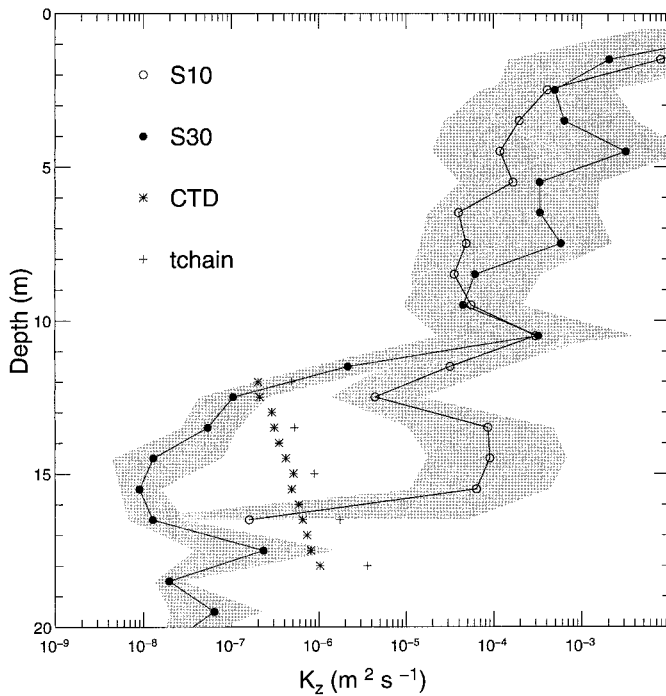


Fig. 8. Profiles of maximum likelihood estimator for K_z at in-shore (\circ) and offshore (\bullet) stations plotted with K_z values obtained with the heat flux method using data from lake-wide CTD profiles ($*$) and from T/chain data ($+$). Shaded area indicates 95% confidence intervals determined from percentile bootstrap. Data from 12 and 13 October are used for the inshore estimate; data from all 3 d are used for the offshore estimate.

data and lake-wide CTD profiles are intermediate to those obtained from microstructure profiling. Values of K_z obtained with the thermistor chain and CTD profiles are consistent with each other. Those from the thermistor chain are only two to four times higher than those obtained from the CTD profiles; K_z values for the second averaging period for the thermistor chain were within 50% of those of the first.

Coefficients of eddy diffusivity obtained from heat flux or tracer measurements integrate over all the processes that cause vertical transports and are average, whole-lake values over the time of sampling. In contrast, coefficients of eddy diffusivity from microstructure measurements provide snapshots of mixing at one location at one instant in time. Time-series data of microstructure profiles obtained at many locations are required to obtain averages comparable to those from heat-flux and tracer methods. However, the large discrepancies we observed between K_z values obtained from our heat-flux measurements and our microstructure measurements suggest that processes occurring inshore are dominating the mixing in the lake.

That K_z values from the middle to the base of the pycnocline offshore were equivalent to the coefficient of molecular conductivity suggests little heat flux occurred at those depths offshore. Further evidence that heat was not transported by turbulence offshore is provided by the comparison of measured values of ϵ with threshold values of ϵ (Figs. 5, 6). The threshold rate of energy dissipation ϵ_{thr} required to support a buoyancy flux in stratified fluids is equal to $15 \nu N^2$

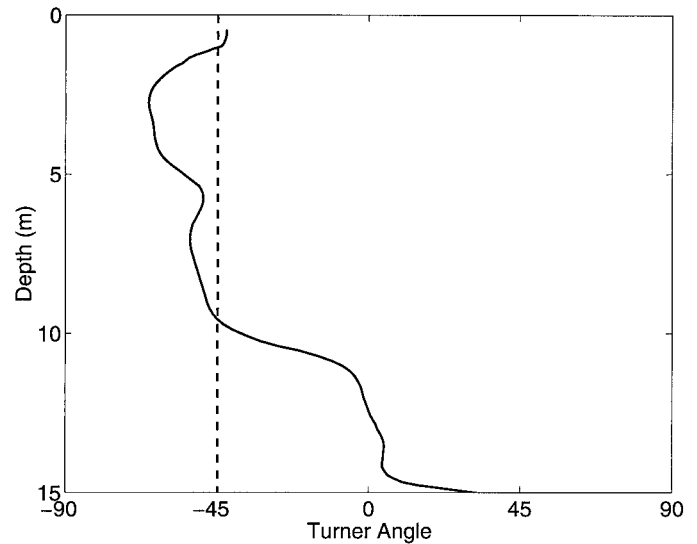


Fig. 9. Turner angle (degrees) vs. depth at S10 on 11 October 1995. CTD data from 0944 h.

(Ivey and Imberger 1991). Below the temperature maximum at the top of the thermocline, ϵ exceeded ϵ_{thr} in only 1% of the segments offshore. In contrast, ϵ was $>\epsilon_{thr}$ in 4% of the segments inshore on 11 October, before the increased turbulence was observed, and in 21% of the segments on 12 and 13 October when enhanced mixing was observed. Etemad-Shahidi and Imberger (pers. comm.), who performed direct measurements of buoyancy flux, found negligible net buoyancy flux within the thermocline at offshore locations within Lakes Biwa and Kinneret. These results also support our contention that K_z values were close to values of molecular conductivity offshore.

Double-diffusive convection did not contribute to enhanced mixing below the top of the thermocline (Fig. 9). Values of the Turner angle (Ruddick 1983) did not fall below -45° , which would indicate double-diffusive instability, and did not exceed 45° , which would indicate salt fingering, in the stably stratified waters below 10 m. In contrast, the Turner angle was less than -45° at depths above the temperature maximum at the top of the thermocline, indicating that mixing may have been enhanced by double diffusion. This pattern was true inshore as well as offshore (data not shown), although the depths of potential double-diffusive instability varied above 10 m.

During our study, the low values of ϵ relative to that required to support mixing in a stratified fluid, the lack of double-diffusive processes in the pycnocline, and K_z values equivalent to molecular rates imply that no heat flux occurred due to turbulent mixing at the offshore site between 13 and 20 m. If heat flux had occurred at molecular rates offshore during the longer time periods covered by the CTD profiling, the heat flux computed from the CTD profiles and temperature chain would have originated from mixing over sloping boundaries or rough topography and subsequent lateral transport.

Time-series profiles of ammonium and chlorophyll—Profiles of temperature, ammonium, and Chl *a* are plotted in

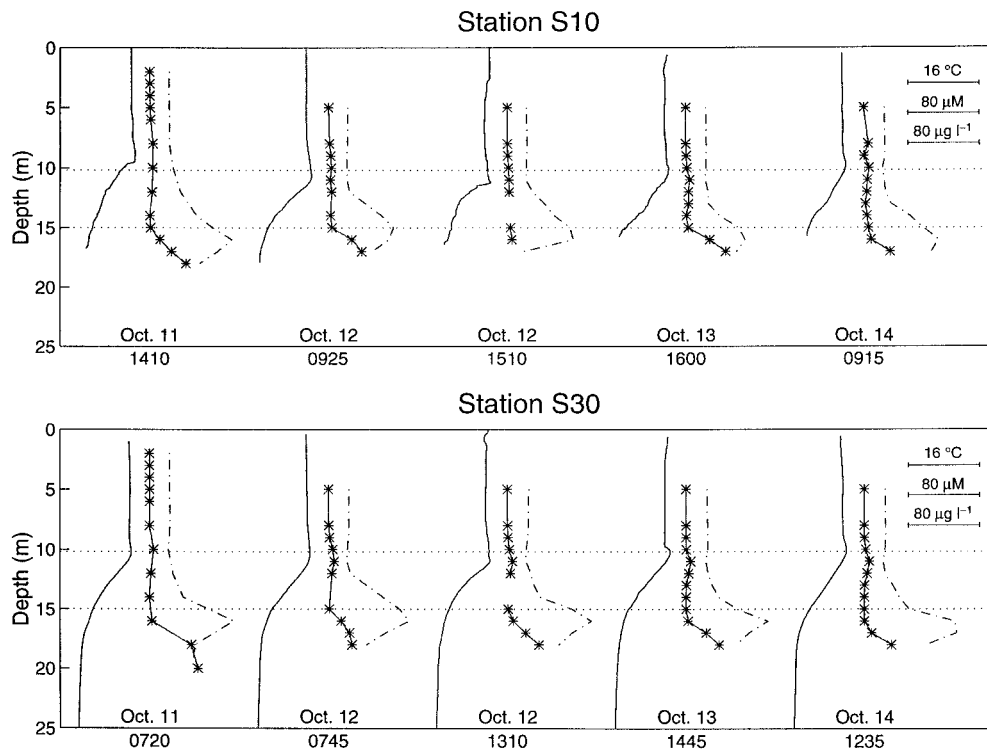


Fig. 10. Profiles of temperature (-), ammonium (*), and Chl *a* (-). Time of nutrient sampling is marked; temperatures were obtained from CTD or microstructure cast within 40 min of sampling, except on 14 October, when CTD profile was taken 3 h earlier. The scale bar in upper right allows determination of change in concentration. Surface temperatures ($^{\circ}\text{C}$) at S10 were 16.0 at 1342 h on 11 October, 15.2 at 0903 h on 12 October, 16.3 at 1514 h on 12 October, 16.0 at 1544 h on 13 October, and 15.2 at 0856 h on 14 October; at S30, they were 15.5 at 0732 h on 11 October, 15.1 at 0707 h on 12 October, 16.0 at 1340 h on 12 October, 16.0 at 1427 h on 13 October, and 14.9 h at 0948 h on 14 October. Ammonium concentrations at 5 m at S10 were 0.92, 0.96, 1.14, 0.51, and $0.38 \mu\text{M}$; at S30, they were 0.39, 0.55, 0.57, 0.25, and $0.53 \mu\text{M}$; Chl *a* concentrations at 5-m depth at S10 were 2.5, 2.7, 2.75, 4.77, and $3.84 \mu\text{g liter}^{-1}$; and at S30, were 2.79, 3.38, 4.77, 3.69, and $4.16 \mu\text{g liter}^{-1}$.

Fig. 10. The depth of the nutricline was consistently 15 m at S10, except at 1510 h on 12 October and on 14 October. Its depth varied between 15 and 16 m offshore. The chlorophyll maximum tended to coincide with the top of the nutricline. That the depths of the nutricline and the chlorophyll maximum were decoupled from changes in the depth of temperature inversion at the top of the thermocline supports our observations in Fig. 4 of phase shifts between internal waves at the top and bottom of the pycnocline.

The data from 1510 h on 12 October provide evidence for mixing at the nutricline. When ammonium is plotted against temperature instead of depth, the influence of internal waves on depth distributions is removed. The ammonium concentrations from 15 m are higher than those along the same temperature isotherm on the previous day, and the concentrations from 16 m are lower (data not shown).

Discussion

Rates of turbulent kinetic energy dissipation in excess of $10^{-6} \text{ m}^2 \text{ s}^{-3}$ occurred in the pycnocline over sloping topography during a period when winds had generated internal waves. The bottom had a slope of 4%, and the pycnocline

intersected the bottom in this region. While the greatest enhancement of energy dissipation rates occurred within 3.5 m of the bottom, enhancement also occurred at other depths within the pycnocline. Offshore, at the same depths, ϵ was $<10^{-8} \text{ m}^2 \text{ s}^{-3}$. These results are indicative of boundary mixing (Ivey et al. 1995; Lemckert and Imberger 1998). Steepening of internal waves after reflection (Eriksen 1998) or flow over topographic features (Thorpe 1984) may have induced the mixing away from the boundary. Boundary mixing can increase nutrient fluxes and primary productivity if it occurs where gradients in nutrient, phytoplankton, or bacterial concentrations are present. Determining the characteristics of the internal wave field during the time the enhanced mixing occurred is essential for predicting the onset of boundary mixing. Estimating the spatial and temporal extent of boundary mixing is essential for predicting its effects on nutrient fluxes and primary productivity.

Internal wave climatology—Analysis of time-series temperature data can provide insights into the mechanisms causing boundary mixing. At present, assessment of dominant mechanisms depends upon comparing field results with analytical and laboratory models and upon comparing results

from other field studies. For instance, based on the rapid loss of potential energy in the internal wave field following a typhoon, boundary mixing has been proposed as the dominant mechanism for dissipating the energy input into the internal wave field in Lake Biwa (Saggio and Imberger 1998). They observed high-frequency waves, which are likely a signature for the onset of mixing or the occurrence of mixing, after shoaling of a mode one Kelvin wave in shallow waters and after compression of the thermocline following a mode two internal jump also associated with shoaling of a Kelvin wave.

We determined the dominant modes of internal waves in Mono Lake and looked for high-frequency waves associated with the mixing events we observed. For the vertical density structure on 12 October 1995, we calculated phase speeds of baroclinic internal wave modes by solving the long-wave form of the internal wave eigenvalue problem following Monismith (1985, 1987). The vertical density structure was approximated with 100 layers. The calculated phase speeds for the first and second vertical modes were 0.68 and 0.21 m s^{-1} , respectively. We also used the equation for phase speed of two- or three-layered systems and varied the assumed depth of the lake to obtain a range of possible phase speeds. The phase speed c for a two-layered system is given by $c = (g(\rho_1 - \rho_2)h_1h_2/(\rho_2(h_1 + h_2)))^{1/2}$, where h is the depth of a layer, and 1 refers to the surface layer and 2 to the deep layer. We let $h_1 = 10$ m and $h_2 = 15$ and 28 m. For a three-layered system, we used the equations in Munnich et al. (1992). For the first vertical first horizontal (V1H1) mode wave, phase speeds ranged from 0.68 to 0.8 m s^{-1} ; for the second vertical first horizontal (V2H1) mode wave, they ranged from 0.21 to 0.23 m s^{-1} . We assumed the effective length of the lake (i.e., the length at the depth of the pycnocline) to be 11 km. Consequently, the calculated frequency band ranged from 0.8 to 0.9 cpd and from 2.6 to 3.1 cpd for the V2H1 and V1H1 wave modes, respectively.

Rotational effects are possible if the internal Rossby radius is less than the length of the lake at the depth of the pycnocline. The internal Rossby radius $R = c/f$, where f , the Coriolis force, $= 8.9 \times 10^{-5} \text{ s}^{-1}$ at 38°N . The inertial frequency is 1.2 cpd. Using the phase speeds above of the first mode wave, R is between 8 and 9 km. Rotation may be important; if so, a Kelvin wave could develop. The frequency at which a Kelvin wave would propagate around a lake depends on its phase speed and the effective circumference of the basin. Assuming that Mono Lake is circular with a surface area of 160 km^2 and that the depth of the 15-m contour is everywhere 1 km from shore, the perimeter of the lake is 37 km. Assuming the Kelvin wave follows the actual 15-m contour everywhere except in the region behind the island gives a perimeter of 52 km. The frequency of the Kelvin wave would be in the range of 1.2–1.9 cpd given these uncertainties.

Spectral densities computed from individual thermistors over 3.8-d intervals (16,384 samples) beginning at 0 h on 11 October, with each subsequent spectra shifted by $\frac{1}{2}$ d, illustrate a pronounced peak centered near 3 cpd at the middle of the pycnocline (Fig. 11a). In addition, they show a peak within the frequency range of the V2H1 internal wave at the beginning of the period at the base of the pycnocline

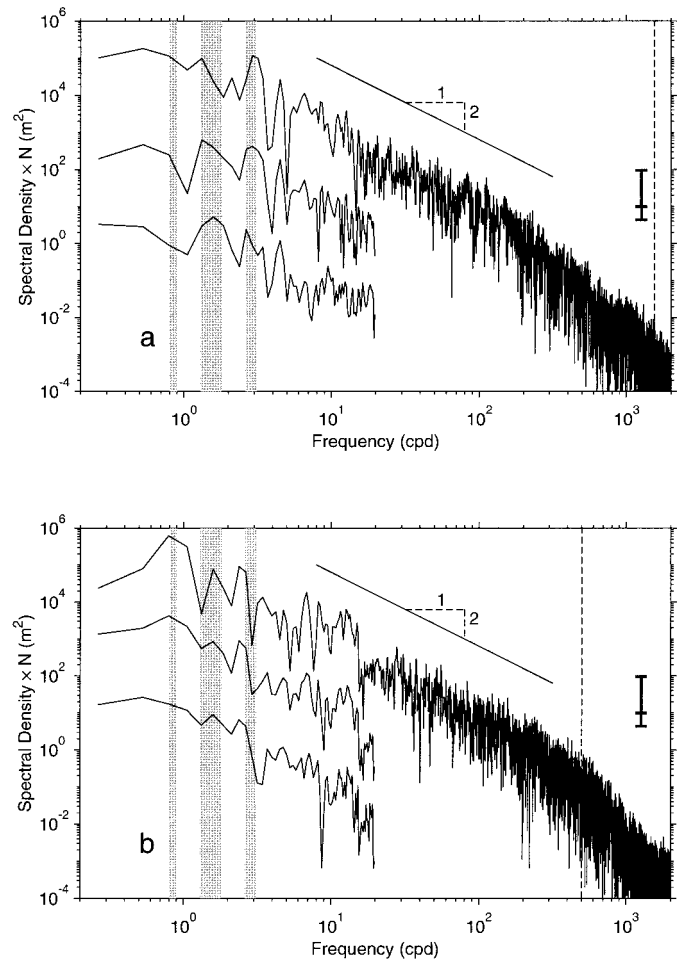


Fig. 11. Power spectra of displacements of the 14°C isotherm scaled with the mean N at each depth. The first spectrum is computed from the 3.8-d record beginning at 0 h on 11 October. The second and third spectra are computed from records starting 12 and 24 h later and are offset by two and four decades, respectively. The bars on the right of the figure indicate the 80% confidence interval. The vertical dashed line indicates the buoyancy frequency at the mean depth of the isotherm. Shaded bands from left to right indicate estimated frequencies for V2H1, Kelvin or V2H2, and V1H1 wave modes as discussed in the text. (b) Same as (a) for the 5°C isotherm.

(Fig. 11b). The results at 12 m are consistent with the fact that the amplitudes of a V1H1 wave would be maximal and the amplitude of a V2H1 wave would be minimal near the middle of the pycnocline. Similarly, the results at 15 m are consistent with the amplitudes of a V1H1 wave being minimal and a V2H1 wave being maximal near the base of the pycnocline.

In addition, the spectra illustrate a peak between 1.3 and 1.8 cpd; while the energy in this range stays nearly constant, it becomes more defined over time from the 6 to the 14°C isotherms (only the 14°C isotherm is shown). The amplitude of this peak is not significant at the base of the pycnocline. It is not possible to define conclusively the mode of this wave; its frequency coincides with that of a V2H2 mode internal wave, a Kelvin wave, or a V1H1 mode wave if such modes propagated from the western to the eastern basin.

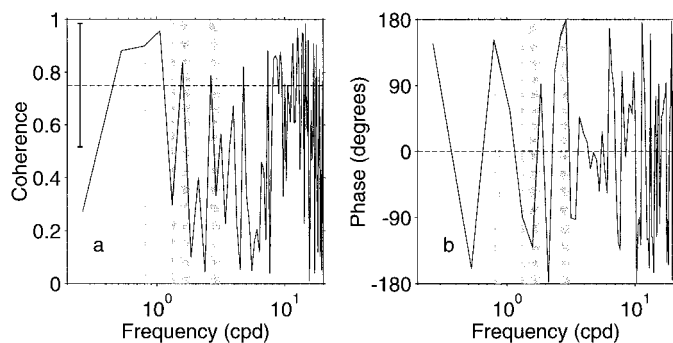


Fig. 12. (a) Magnitude-squared of coherence, and (b) relative phase for 14 and 5°C isotherm displacements. The error bar for the coherence spectrum represents the 80% confidence limits for a coherence value of 0.75 (the dotted line). Values > 0.75 have a small estimated error. If the coherence estimate is > 0.75 , we can be 80% confident that the actual coherence is greater than an acceptable threshold value of 0.5. As in Fig. 11, shaded bands indicate estimated frequencies for V2H1, Kelvin or V2H2, and V1H1 wave modes.

If the peaks in the range of 0.8–0.9 cpd were indicative of a second vertical mode internal wave, they would be coherent but 180° out of phase between the top and base of the pycnocline. Because of the temperature inversion at the top of the pycnocline, isotherm displacements cannot be computed there. Consequently, we can only look for coherent motions from the middle to the base of the pycnocline. Coherence spectra indicate that motions in the range from 0.8 to 0.9 cpd are coherent and are 150° out of phase (Fig. 12). These results are suggestive of a second vertical mode response. In addition, the CTD transect between S10 and ET5.6 on 12 October indicated that the tilting that occurred at both interfaces was in opposing directions.

Through much of its range, the slope of the internal wave spectral density scales with frequency to the -2 power (Fig. 11a,b). This slope is comparable to that found in the Garrett and Munk spectra for the ocean (Gregg 1987) and in Lake Biwa (Saggio and Imberger 1998). Due to superposition of linear internal waves, a -2 slope is expected from the inertial to the buoyancy frequency (Saggio and Imberger 1998). Departures from this slope may be indicative of other processes.

Critical frequencies for internal wave breaking—The critical frequency at which shoaling of internal waves is expected can be determined from bottom slope, β , and the buoyancy frequency using the expression $f_c = N\beta$ (Ivey et al. 1995). Enhancement of energy at the critical frequency has been observed by Eriksen (1998) and Van Haren et al. (1994), with the broadening of the peak attributed to wave reflection and breaking. Based on N varying from 20 to 70 cph in the pycnocline (Fig. 3a) and β varying from 0.1 to 0.01 near S10, the range of critical frequencies at our near-shore site was 2–168 cpd. This broad range may preclude enhancement at a defined range. However, with the exception of the spectral densities of isotherm displacements at 5°C, spectral densities for other isotherm displacements in the pycnocline rolled off at a higher slope than -2 at fre-

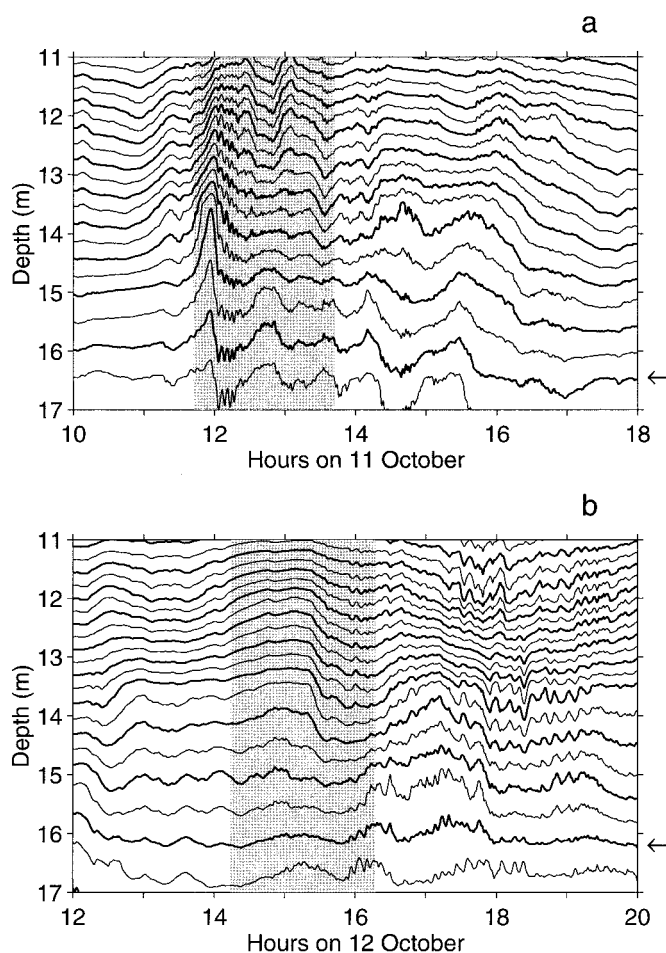


Fig. 13. (a) Isotherm displacements from 10 to 18 h on 11 October 1995. Gray band indicates the time period over which microstructure profiling was conducted at S10. Arrow indicates the location of the 6°C isotherm. Isotherms are in 0.5°C intervals. (b) As in (a) but for 12–20 h on 12 October 1995.

quencies higher than 200 cpd (Fig. 11). However, the rolloff may be due to the response time of the sensors. All spectra showed peaks between the frequency of the first vertical first horizontal internal wave and 20 cpd, with those from the 5°C isotherm displacements enhanced relative to what would be expected if the rolloff were to follow the -2 slope.

The mixing events we observed near the boundary occurred subsequent to compression of the thermocline (Fig. 4; morning of 12 October). At that time, the depth difference between the 5 and 14°C isotherms was only 5 m; the distance tended to average 7 m. In addition, the amplitude of the internal waves between 14- and 18-m depths (5–8°C isotherms) rapidly increased. Waves with a frequency of 100 cpd occurred on the crest (data not shown). As the internal wave subsided, a wave train whose frequency was 35 cpd occurred between 14.5 and 16 m (Fig. 13b). We observed the intense mixing at those depths at that time at our near-shore site. Subsequent to our observed mixing events, even higher frequency (130 cpd) waves were observed. Amplitudes of one of these high-frequency wave packets, located between 13.5 and 15 m, ranged from 5 to 12 cm. That en-

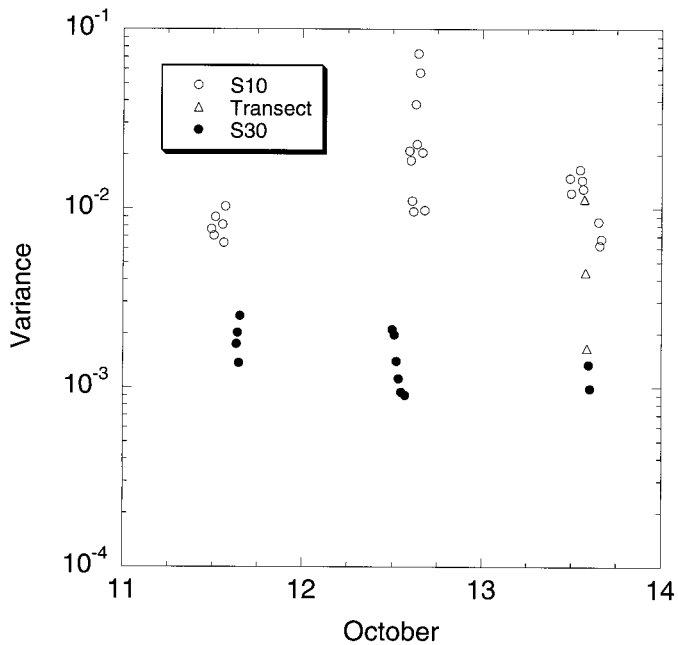


Fig. 14. Variance ($^{\circ}\text{C}^2$) of temperature profiles at inshore (S10), offshore (S30), and along transect (Δ) from S10 to S30 for the 3 d of sampling. On transect (Figs. 1, 2), profile from 1342 h has the most variance; that from 1405 h has the least; profile from 1352 h was intermediate.

hanced mixing was not observed on 11 October, when high-frequency waves (200–300 cpd) developed following the initial tilting of the thermocline (Fig. 13a) suggests that the mixing we observed was associated with the increased shears due to constriction of the thermocline associated with passage of a second mode internal wave. Since the Rossby radius of deformation in Mono Lake is comparable to the width of the basin, we cannot say definitively that a Kelvin wave formed. However, Thorpe's (1998) analysis indicates that rotation of basin scale modes is likely whenever lakes have shallow areas. Consequently, it is likely that a rotating, second vertical mode wave occurred, and the mixing we observed was associated with its interaction with the boundary and the formation of waves with frequencies in the range critical for wave breaking.

More high-frequency wave packets occurred throughout the pycnocline on 12 and 13 October than on 11 October, and their amplitudes were greater. Since the energy in the internal wave field is proportional to amplitude squared, and given that some of the increase in potential energy due to mixing was transferred to these high-frequency waves, these observations imply more energy would have been dissipated by mixing on 12 and 13 October than on 11 October. These observations are in accord with our measurements of ϵ . In addition, the frequency of the waves observed at noon on 11 October was greater than critical.

The frequencies of waves generated after the compression of the thermocline span the range of frequencies predicted to be critical for wave breaking in the pycnocline. Assuming that these waves will break, we can compute the expected dissipation rates. We assume that the potential energy in

these wave packets is dissipated on a time scale comparable to their lifetimes and that the energy is dissipated in a 3.5-m-thick boundary layer. The potential energy per unit mass is $N^2\xi^2$, where ξ is the root mean square displacement (Moum et al. 1992). The volume of the boundary layer is $2.7 \times 10^5 \text{ m}^3$, given a 3.5-m-thick boundary layer, a 1.5-m vertical dimension of the wave packets, and the perimeter of the basin at 15 m = 52 km. The volume of the lake in each of the 1.5-m-thick bands was $1.4 \times 10^8 \text{ m}^3$. On a lake-wide basis, dissipation would have occurred in 0.2% of the volume. We will assume the same percentage in the onshore regions. Given that N at 15-m depth = 0.07 s^{-1} , $\xi = 0.1 \text{ m}$, the energy was dissipated in only 0.2% of the lake volume at that depth, and the lifetime of the wave packet was 9,500 s, $\epsilon = 3 \times 10^{-6} \text{ m}^2 \text{ s}^{-3}$. Similarly, for the wave packet between 13.5 and 15 m that persisted from 1730 to ~ 1930 h, assuming that $N = 0.08 \text{ s}^{-1}$, $\xi = 0.1 \text{ m}$ at 13.5 m, the lifetime of the wave packet was 6,000 s, and the volume involved was 0.2% of the lake volume, $\epsilon = 5 \times 10^{-6} \text{ m}^2 \text{ s}^{-3}$. For the 0.05-m waves at that time, the calculated dissipation was $1 \times 10^{-6} \text{ m}^2 \text{ s}^{-3}$. These estimates are comparable to the higher values of ϵ that we measured and indicate that breaking of waves at critical frequencies could have led to the enhanced mixing in the boundary.

Maxworthy et al.'s (1998) experimentation and observations from Lake Biwa indicated that when basin scale modes interact with topography, mixing occurs followed by high-frequency waves in the pycnocline. They hypothesized that the mixing occurs when a Kelvin wave becomes unstable as its amplitude increases with contact with the boundary. Alternatively, as proposed by Horn, Imberger, and Ivey (pers. comm.), solitary waves, conoidal waves, or undular bores that break against the boundary are formed after basin scale waves steepen nonlinearly. Saggio and Imberger (1998) noted an increase in energy in the high-frequency wave band after compression of the thermocline due to passage of a Kelvin wave. Our results suggest that these high-frequency waves break, causing enhanced dissipation in nearshore areas.

Both the peninsula associated with Rush Creek and the topographic features to the east of S10 could also create instabilities in rotating basin scale modes. Any near-bottom currents flowing over topography could also contribute a flux of energy to the wave field. Following the analysis of Toole et al. (1997) derived from Bell (1975), the rate of energy input into the wave field due to topographic features of height H and wavelength L is $\frac{1}{8} \rho \pi u^2 N H^2 L^{-1}$, where u is current speed. Two topographic features are to the east of S10. One is 5 m high and 100 m in cross-section, and the other is 10 m high and 500 m in cross-section. Assuming current speeds of 0.05 ms^{-1} and an N value = 0.08 s^{-1} in the middle of the pycnocline gives an energy input of $2 \times 10^{-2} \text{ W m}^{-2}$. If the current speeds were 0.01 ms^{-1} , the energy input would be two orders of magnitude lower. If this flux is dissipated throughout the 10-m-thick pycnocline, dissipation rates between 10^{-8} and $10^{-6} \text{ m}^2 \text{ s}^{-3}$ are predicted. Similar results are obtained based on the peninsula due to Rush Creek. These calculations indicate that formation of lee waves by topographic features could contribute to the mixing, including that away from the boundary.

Internal wave strain—An increase in the steplike structures in density profiles is an indicator of the internal wave strain (Gregg and Kunze 1991) that would result from reflection or interactions of the density field with lee waves. The greater number of steps in our temperature profiles (i.e., 10-cm scale regions with high-temperature gradients followed by regions with low) inshore compared to offshore, suggests that internal wave strain contributed to the turbulence inshore. To quantify this effect, we filtered our temperature profiles below the depth of the warm layer and above 17 m offshore, the depth of the profile inshore, with a 10-point moving average applied recursively. This filter removed the fluctuations in the temperature profile due to the turbulent mixing regions. We subsequently subtracted this filtered profile from one obtained with a 500-point moving average applied recursively. We then computed the variance. Offshore, the variance ranged from 1×10^{-3} to $3 \times 10^{-3} \text{ }^\circ\text{C}^2$ for all 3 d (Fig. 14). In contrast, the variance inshore ranged from 6×10^{-3} to $8 \times 10^{-2} \text{ }^\circ\text{C}^2$, with the largest range on 12 October. The variance was higher for the profiles taken during the morning and early afternoon of 12 October than for the three taken 2–3 h later. The variance decreased in temperature profiles taken on a transect from S10 to S30 (Figs. 1, 2); 0.4 km away from S10, where the bottom slope β was 1%, it was comparable to that at S10. It decreased by a factor of two 0.6 km from S10, where β again = 1%. At a distance 1.1 km away from S10, where $\beta = 0.5\%$, the variance in the temperature profile was comparable to that at S30. In consequence, if the distortion of the temperature profile was due to straining of the internal wave field, the effects are limited. The increased wave strain and associated mixing can increase the lake-wide effects of boundary mixing on nutrient and particle fluxes.

Spatial extent of boundary mixing—Estimating where boundary mixing leads to enhanced nutrient and particle fluxes is critical for assessing its role in the functioning of lacustrine ecosystems. For instance, while we observed moderate turbulence ($\epsilon \leq 10^{-7} \text{ m}^2 \text{ s}^{-3}$) in the bottom 10 m at S30, any nutrients or heat mixed vertically in this region would not be transferred through the pycnocline above. Transport through the pycnocline occurred at the lake margins.

As a first approximation, we can estimate where boundary mixing can cause vertical transports by considering where the pycnocline is in contact with a boundary. Neglecting pycnocline displacements and given that the pycnocline was 10 m thick, boundary mixing could occur in 30% of the basin. Using the detailed bathymetry of the lake, assuming that the most intense mixing occurred within 3 m of a sloping boundary, and knowing that the nutricline was at 15-m depth, we estimate that nutrient fluxes from the nutricline would occur over an area equal to 6% of the basin. Fluxes from entrainment of pore waters would occur wherever stratified waters were in contact with a sloping bottom. For $N^2 > 10^{-5} \text{ s}^{-2}$, $\beta > 1\%$, and depth > 15 m, such entrainment could occur in 17% of the lake. The percentage of the lake basin affected would depend on seasonal stratification and wind direction.

The comparison of K_z values from microstructure and

from the heat-flux method can be used to determine the combined spatial-temporal extent of boundary mixing. Between 13.5- and 15.5-m depths, K_z values were $10^{-8} \text{ m}^2 \text{ s}^{-1}$ offshore and $10^{-4} \text{ m}^2 \text{ s}^{-1}$ inshore, and spatially averaged values were $10^{-6} \text{ m}^2 \text{ s}^{-1}$. The total flux over time at these depths, $F_T A_T \tau = F_I A_I \tau_I + F_O A_O \tau_O$, where F is flux, A is area, τ is time, T represents total, I represents inshore, and O represents offshore. If the gradient in heat or solutes is the same inshore as offshore, the equation becomes $K_{zT} A_T \tau = K_{zI} A_I \tau_I + K_{zO} A_O \tau_O$. Assuming that offshore fluxes were negligible, solution of the equation indicates that the time and space over which boundary mixing occurred would only be 1% of the lake area times the time considered. If arithmetic averages of K_z or lower values of mixing efficiency are used in the calculation, the estimate could reach 20%. Clearly, the mixing occurs in intermittent pulses.

Predicting boundary mixing using Lake numbers—Predicting the frequency of boundary mixing events depends on assessing the wind stress likely to set up pycnocline tilting relative to the resisting force due to the stratification within the pycnocline. To compare these forces, we computed the Wedderburn number W and the Lake number L_N (Imberger and Patterson 1990). Stevens and Imberger (1996) suggested that the Lake number is the more general of the two, as it integrates over the entire volume of the lake. Both numbers have been used to predict upwelling and the modal response of the lake. Monismith's (1985, 1986, 1987) laboratory and field experiments predicted internal wave tilting for different W 's; Imberger and Patterson (1990) reevaluated Monismith's experiments using the Lake number. For $L_N > 10$, tilting of the base of the pycnocline would not occur, whereas for $L_N < 10$, the lower interface would tilt. For both $W < 1$ and $L_N < 1$, a first vertical mode response occurred, with both interfaces tilting and remaining parallel. In contrast, where both W and L_N were between 1 and 10, the upper interface showed tilting and a second vertical mode response, but the lower interface remained horizontal.

Wedderburn and Lake number values for 10–14 October 1995 were calculated using hourly averaged wind speeds (Fig. 15). Because the patterns for these two numbers were essentially the same, we will restrict our discussion to L_N . Winds on 10 October led to $L_N = 5$. On 11 October, when wind speeds averaged 10–11 m s^{-1} , L_N dropped to 2. Initially, the entire pycnocline tilted (Fig. 4). Subsequently, when the wind ceased, L_N exceeded 100. When wind speeds increased on 12 October, L_N dropped to a low of 4. Pycnocline response to winds that change direction and magnitude is more complex than those in controlled laboratory settings. Results of our spectral analysis suggest development of first and second vertical modes and possibly a Kelvin wave within the pycnocline. In contrast to Imberger and Patterson's (1990) predictions, L_N and W between 1 and 5 can lead to tilting of both the upper and lower portions of the pycnocline and complex modal response throughout the pycnocline.

Despite the low L_N on 10 and 11 October, boundary mixing was not observed until 12 October. The delayed response suggests a time lag between the wind impulse beginning the event and the development of conditions conducive to

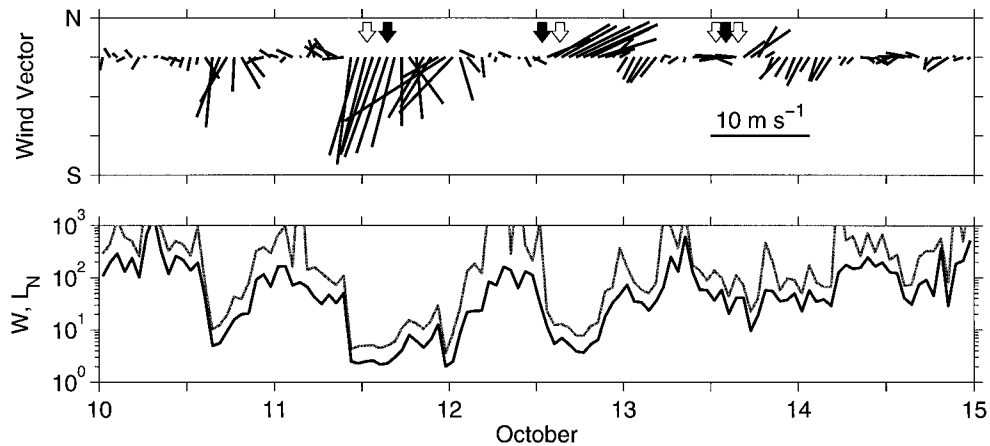


Fig. 15. Wind vectors (top panel) and (bottom panel) Wedderburn numbers (upper gray line) and Lake numbers (lower black line) from 0000 h on 10 October through 2400 h on 14 October. Wind vectors show vector-averaged wind velocities for 1-h periods. Wedderburn and Lake numbers are calculated from hourly wind speeds. Microstructure profiles were taken at periods indicated by arrows, with open arrows denoting inshore profiles.

boundary mixing. Steepening of a basin scale mode appears to be critical.

Initiation of boundary mixing may also require that low values of L_N persist. The length of time likely depends on $T/4$, the time for tilt to develop, where T is the wave period (Stevens and Imberger 1996). For the first vertical mode, $T/4$ is ~ 2 h; for the second, ~ 6 . The longer interval is supported by the fact that the intense mixing we observed was initiated by two 7-h wind events. The decreasing likelihood of boundary mixing events as water-column stability increases is indicated in MacIntyre and Romero's (in press) calculations of L_N from 1992 to 1996.

Biological consequences of boundary mixing—The importance of boundary mixing to a lake's productivity depends on the depths where it occurs. If it occurs at the nutricline, nutrients from below will be mixed into the overlying water. If it occurs above the nutricline and is of sufficient intensity to disturb the sediments, nutrients in the pore waters may be mixed upward. Similarly, particles and phytoplankton will be mixed upward.

In Mono Lake, as in many waterbodies (Moll et al. 1984; Coon et al. 1987), the nutricline is located within the metalimnion, and a deep chlorophyll maximum occurs above it. Consequently, nutrient fluxes from boundary mixing at the nutricline will serve to supply phytoplankton in the chlorophyll maxima. For instance, in Mono Lake, the upward fluxes of ammonium at the nutricline were $28 \text{ mmol m}^{-2} \text{ d}^{-1}$ on 12 October and $3 \text{ mmol m}^{-2} \text{ d}^{-1}$ on 13 October.

Daily rates of primary productivity are generally between 0.5 and 2.0 g C m^{-2} during the summer in Mono Lake (Jellison and Melack 1993a), with 5–10% occurring in the deep chlorophyll maximum (Culbertson pers. comm.). Assuming that boundary mixing occurs over 10% of the area of the lake in contact with the nutricline and that offshore fluxes are molecular, the total lake-wide flux on 12 October would have been $2.8 \text{ mmol m}^{-2} \text{ d}^{-1}$. Using a C:N molar ratio of 6, this flux could sustain $16.8 \text{ mmol m}^{-2} \text{ d}^{-1}$ of primary

production, or $0.2 \text{ gCm}^{-2} \text{ d}^{-1}$. Similarly, the flux on 13 October could sustain $0.02 \text{ gCm}^{-2} \text{ d}^{-1}$. Hence, the fluxes of ammonium by boundary mixing are sufficient to support daily rates of primary productivity within the deep chlorophyll maximum. Because the water column was anoxic at 14-m depth on 12 October, it is unlikely that *A. monica* would have grazed at those depths and contributed to the ammonium supply by excretion. Consequently, boundary mixing may be the dominant mechanism supplying ammonium to the deep chlorophyll maximum.

Because elevated mixing rates occurred within and above the deep chlorophyll maximum, phytoplankton would have been mixed upward and exposed to higher irradiances. Using Platt et al.'s (1980) relation for photosynthesis as a function of irradiance, together with values of the maximum rate of photosynthesis per unit chlorophyll (P_{\max}) and the initial slope α of the light-limited portion of the photosynthesis vs. irradiance curve (Jellison and Melack 1988), we calculated that photosynthetic rates would have doubled as phytoplankton were mixed from 14 to 12 m in Mono Lake. Consequently, when boundary mixing occurs at the depth of the deep chlorophyll maximum, it maintains nonmotile phytoplankton in the euphotic zone by periodically mixing them upward. The combination of increases in nutrient flux and increases in the dosage of irradiance results in enhanced rates of primary productivity.

Increased nutrient fluxes could occur at the top of the pycnocline if shears entrained sediments and associated pore waters or if partial upwelling occurred. Sediment resuspension has been observed due to boundary mixing (Gloor et al. 1994), but no study has yet examined the contribution of boundary mixing to entrainment of pore waters. Ostrovsky et al. (1996) attribute the localized increases in fish and chlorophyll in nearshore waters of Lake Kinneret to upwelling in combination with boundary mixing.

Two-dimensional paradigm for vertical fluxes—Our measurements of turbulence and associated fluxes highlight the

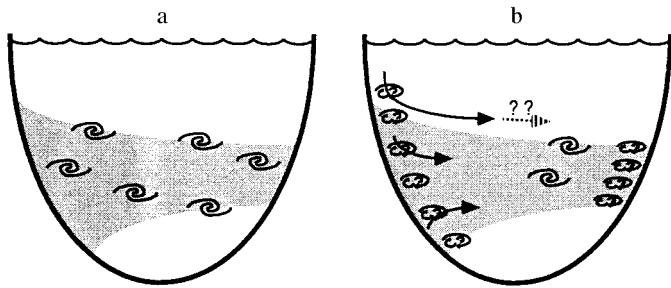


Fig. 16. (a) One-dimensional model of mixing in the metalimnion in which billows (gravitational instabilities) are assumed to cause all the vertical transport. (b) Two-dimensional model, in which some vertical transport occurs via billowing in the metalimnion but is dominated by turbulence occurring over sloping or rough boundaries. Currents or intrusions (arrows) provide lateral transport of solutes and particles entrained from the sediments or nutricline near the boundary into the pelagic zone.

importance of boundary mixing for nutrient supply in stratified lakes and provide evidence, along with the results of Wüest et al. (1996) and Lueck and Mudge (1997), for the need to revise the paradigm describing the flux of heat or nutrients in stratified waterbodies. Under the one-dimensional paradigm, the upward flux of nutrients was believed to occur via mixing in turbulent eddies occurring throughout the metalimnion (Fig. 16a). However, our comparison of mixing events at an inshore and an offshore site at Mono Lake showed that turbulent intensities as indicated by ϵ , K_z values, and calculated nutrient fluxes were two to four orders of magnitude higher where the thermocline intercepted a sloping boundary. Because of the localized nature of boundary mixing, description of the movement of solutes and particles is best described as a two-step process: (1) boundary mixing causes vertical flux near the margins of the lake, and (2) currents advect material into the open water (Fig. 16b). Horizontal current speeds and lake size determine whether the nutrients or the phyto- or bacterioplankton that have taken them up remain in the littoral or are swept offshore.

Our microstructure measurements, in combination with profiles of ammonium and assessment of temporally and spatially averaged values of the coefficient of eddy diffusivity, indicate that boundary mixing is important for nutrient fluxes and the resulting primary productivity in Mono Lake. Boundary mixing is the dominant mechanism supplying nutrients to the chlorophyll maxima in the lake and leads to enhanced productivity due to both the flux of nutrients and the upward flux of phytoplankton. We propose that it supplies nutrients to the upper part of the euphotic zone by entrainment of pore waters. Boundary mixing was initiated when Lake numbers dropped to 2. The thermocline was compressed, and the amplitude of basin scale internal waves rapidly steepened, followed by the generation of high-frequency waves critical for breaking. Using these insights, the frequency of mixing at the boundaries of other lakes can be predicted, and ultimately, improved models of lake primary productivity will be developed that include nutrient fluxes as affected by basin morphometry and local climate.

References

- ANIS, A., AND J. N. MOUM. 1994. Prescriptions for heat flux and entrainment rates in the upper ocean during convection. *J. Phys. Oceanogr.* **24**: 2142–2155.
- , AND ———. 1995. Surface wave–turbulence interactions—scaling $\epsilon(z)$ near the sea surface. *J. Phys. Oceanogr.* **25**: 2025–2045.
- BAKER, M. A., AND C. H. GIBSON. 1987. Sampling turbulence in the stratified ocean: Statistical consequences of strong intermittency. *J. Phys. Oceanogr.* **17**: 1817–1836.
- BELL, T. H. 1975. Lee waves in stratified flows with simple harmonic time dependence. *J. Fluid Mech.* **67**: 705–722.
- BENDAT, J. S., AND A. G. PERSOL. 1986. *Random data: Analysis and measurement procedures*. Wiley.
- CARTER, G. D., AND J. IMBERGER. 1986. Vertically rising microstructure profiler. *J. Atmos. Oceanic Technol.* **3**: 462–471.
- COON, T. G., M. LOPEZ, P. J. RICHERSON, T. M. POWELL, AND C. R. GOLDMAN. 1987. Summer dynamics of the deep chlorophyll maximum in Lake Tahoe. *J. Plankton Res.* **9**: 327–344.
- DILLON, T. M., AND D. R. CALDWELL. 1980. The Batchelor spectrum and dissipation in the upper ocean. *J. Geophys. Res.* **85**: 1910–1916.
- DIXON, P. M. 1993. The bootstrap and the jackknife: Describing the precision of ecological indices, p. 290–318. *In* S. M. Scheiner and J. Gurevitch [eds.], *Design and analysis of ecological experiments*.
- ERIKSEN, C. C. 1982. Observations of internal wave reflection off sloping bottoms. *J. Geophys. Res.* **87**: 525–538.
- . 1985. Implications of ocean bottom reflection for internal wave spectra and mixing. *J. Phys. Oceanogr.* **15**: 1145–1156.
- . 1998. Internal wave reflection and mixing at Fieberling Guyot. *J. Geophys. Res.* **103**: 2977–2994.
- FOZDAR, F. M., G. J. PARKER, AND J. IMBERGER. 1985. Matching temperature and conductivity sensor response characteristics. *J. Phys. Oceanogr.* **15**: 1557–1569.
- GARRETT, C. 1991. Marginal mixing theories. *Atmosphere-Ocean* **29**: 313–339.
- GLOOR, M., A. WÜEST, AND M. MÜNNICH. 1994. Benthic boundary mixing and resuspension induced by internal seiches. *Hydrobiologia* **284**: 59–68.
- GOLTERMAN, H. L. [ED.]. 1969. *Methods for chemical analysis of fresh waters*. International biological program handbook 8. Blackwell.
- GREGG, M. C. 1987. Diapycnal mixing in the thermocline: A review. *J. Geophys. Res.* **92**: 5249–5286.
- , AND E. KUNZE. 1991. Shear and strain in Santa Monica Basin. *J. Geophys. Res.* **96**: 16709–16720.
- IMBERGER, J. 1994. Transport processes in lakes: A review, p. 99–193. *In* R. Margalef [ed.], *Limnology now: A paradigm of planetary problems*. Elsevier.
- , AND G. IVEY. 1991. On the nature of turbulence in a stratified fluid. Part 2: Application to lakes. *J. Phys. Oceanogr.* **21**: 659–680.
- , AND J. C. PATTERSON. 1990. Physical limnology. *Adv. Appl. Mech.* **27**: 303–475.
- IVEY, G. N., P. DE SILVA, AND J. IMBERGER. 1995. Internal waves, bottom slopes and boundary mixing, p. 199–206. *In* Proceedings eighth 'Aha Huliko'a Hawaiian Winter Workshop, Flow-topography interactions. Univ. of Hawaii.
- , AND J. IMBERGER. 1991. On the nature of turbulence in a stratified fluid. Part 1: The efficiency of mixing. *J. Phys. Oceanogr.* **21**: 650–658.
- JASSBY, A., AND T. M. POWELL. 1975. Vertical patterns of eddy diffusion during stratification in Castle Lake, California. *Limnol. Oceanogr.* **38**: 1008–1019.

- JELLISON, R. S. 1993. Limnology of hypersaline Mono Lake, California, during the onset, persistence and breakdown of meromixis. Ph.D. thesis, Univ. of California-Santa Barbara.
- , S. MACINTYRE, AND F. J. MILLERO. Density and conductivity properties of Na-CO₃-Cl-SO₄ brine from Mono Lake, California. *Int. J. Salt Lake Res.* In press.
- , AND J. M. MELACK. 1988. Photosynthetic activity of phytoplankton and its relation to environmental factors in hypersaline Mono Lake, California. *Hydrobiologia* **158**: 69–88.
- , AND ———. 1993a. Algal photosynthetic activity and its response to meromixis in hypersaline Mono Lake, California. *Limnol. Oceanogr.* **38**: 818–837.
- , AND ———. 1993b. Meromixis in hypersaline Mono Lake, California. 1: Vertical mixing and density stratification during the onset, persistence, and breakdown of meromixis. *Limnol. Oceanogr.* **38**: 1008–1019.
- , L. MILLER, J. M. MELACK, AND G. L. DANA. 1993. Meromixis in hypersaline Mono Lake, California. 2: Nitrogen fluxes. *Limnol. Oceanogr.* **38**: 1020–1039.
- LEDWELL, J. R., AND B. M. HICKEY. 1995. Evidence for enhanced boundary mixing in the Santa Monica Basin. *J. Geophys. Res.* **100**: 20665–20679.
- LEMCKERT, C., AND J. IMBERGER. 1998. Turbulent benthic boundary layer mixing events in freshwater lakes, p. 503–516. *In* J. Imberger [ed.], *Physical processes in lakes and oceans*. Coastal and Estuarine Studies 54. AGU.
- LEMMIN, U. 1987. The structure and dynamics of internal waves in the Baldeggersee. *Limnol. Oceanogr.* **32**: 43–61.
- LUECK, R. G., AND T. D. MUDGE. 1997. Topographically induced mixing around a shallow seamount. *Science* **276**: 1831–1833.
- MAAS, L. R., AND F-P. A. LAM. 1995. Geometric focussing of internal waves. *J. Fluid Mech.* **300**: 1–41.
- MACINTYRE, S. 1998. Turbulent mixing and resource supply to phytoplankton, p.561–590. *In* J. Imberger [ed.], *Physical processes in lakes and oceans*. Coastal Estuarine Studies 54. AGU.
- , AND J. R. ROMERO. Predicting upwelling, boundary mixing, and nutrient fluxes in lakes. *Verh. Int. Verein. Limnol.* In press.
- MASON, D. M. 1967. Limnology of Mono Lake, California. *Univ. Calif. Publ. Zool.* **83**: 1–110.
- MAXWORTHY, T., J. IMBERGER, AND A. SAGGIO. 1998. A laboratory demonstration of a mechanism for the production of secondary, internal gravity-waves in a stratified fluid, p. 261–270. *In* J. Imberger [ed.], *Physical processes in lakes and oceans*. Coastal and Estuarine Studies 54. AGU.
- MOLL, R. A., M. Z. BRAHCE, AND T. P. PETERSON. 1984. Phytoplankton dynamics within the subsurface chlorophyll maximum of Lake Michigan. *J. Plankton Res.* **6**: 751–766.
- MONISMITH, S. G. 1985. Wind-forced motions in stratified lakes and their effect on mixed-layer shear. *Limnol. Oceanogr.* **30**: 771–783.
- . 1986. An experimental study of the upwelling response of stratified reservoirs to surface shear stress. *J. Fluid Mech.* **171**: 407–439.
- . 1987. The modal response of reservoirs to wind stress. *J. Hydrol. Div. ASCE* **113**: 1290–1326.
- MOUM, J. N., D. HERBERT, C. A. PAULSON, AND D. R. CALDWELL. 1992. Turbulence and internal waves at the equator. Part I: Statistics from towed thermistors and a microstructure profiler. *J. Phys. Oceanogr.* **22**: 1330–1345.
- MUNK, W. H. 1966. Abyssal recipes. *Deep-Sea Res.* **13**: 707–713.
- MUNNICH, M., A. WÜEST, AND D. M. IMBODEN. 1992. Observations of the second vertical mode of the internal seiche in an alpine lake. *Limnol. Oceanogr.* **37**: 1705–1719.
- OAKEY, N. S. 1985. Statistics of mixing parameters in the upper ocean during JASIN Phase 2. *J. Phys. Oceanogr.* **15**: 1662–1675.
- OSBORN, T. R. 1980. Estimates of the rate of vertical diffusion from dissipation measurements. *J. Phys. Oceanogr.* **10**: 83–89.
- OSTROVSKY, I., Y. Z. YACOBI, P. WALLINE, AND I. KALIKHMAN. 1996. Seiche-induced mixing—its impact on lake productivity. *Limnol. Oceanogr.* **41**: 323–332.
- PLATT, T., C. L. GALLEGOS, AND W. G. HARRISON. 1980. Photo-inhibition of photosynthesis in natural assemblages of phytoplankton. *J. Mar. Res.* **38**: 687–701.
- POLZIN, K. L., J. M. TOOLE, J. R. LEDWELL, AND R. W. SCHMITT. 1997. Spatial variability of turbulent mixing in the abyssal ocean. *Science* **276**: 93–96.
- ROMERO, J. R., R. JELLISON, AND J. M. MELACK. 1998. Stratification, mixing, and upward ammonium flux in hypersaline Mono Lake, California. *Arch. Hydrobiol.* **142**: 283–315.
- , AND J. M. MELACK. 1996. Sensitivity of vertical mixing in a large saline lake to variations in runoff. *Limnol. Oceanogr.* **41**: 955–965.
- RUDDICK, B. 1983. A practical indicator of the stability of the water column to double-diffusive activity. *Deep-Sea Res.* **30**: 1105–1107.
- , D. WALSH, AND N. OAKEY. 1997. Variations in apparent mixing efficiency in the North Atlantic Central Water. *J. Phys. Oceanogr.* **27**: 2589–2605.
- SAGGIO, A., AND J. IMBERGER. 1998. Internal wave weather in a stratified lake. *Limnol. Oceanogr.* **43**: 1780–1795.
- SIEDLER, G., AND U. PAUL. 1991. Barotropic and baroclinic tidal currents in the Eastern Basins of the North Atlantic. *J. Geophys. Res.* **96**: 22259–22271.
- STEVENS, C., AND J. IMBERGER. 1996. The initial response of a stratified lake to a surface shear stress. *J. Fluid Mech.* **312**: 39–66.
- STRICKLAND, J. S. H., AND T. R. PARSONS. 1972. A practical handbook of seawater analysis. *Bull. Fish. Res. Board Can.* **167**: 1–130.
- TAYLOR, J. R. 1993. Turbulence and mixing in the boundary layer generated by shoaling internal waves. *Dyn. Atmos. Oceans* **19**: 233–258.
- THORPE, S. A. 1984. A laboratory study of stratified accelerating shear flow over a rough boundary. *J. Fluid Mech.* **138**: 185–196.
- . 1987. On the reflection of a train of finite-amplitude internal waves from a uniform slope. *J. Fluid Mech.* **178**: 279–302.
- . 1998. Some dynamical effects of the sloping sides of lakes, p. 441–460. *In* J. Imberger [ed.], *Physical processes in lakes and oceans*. Coastal and Estuarine Studies 54. AGU.
- TOOLE, J. M., K. L. POLZIN, AND R. W. SCHMITT. 1994. Estimates of diapycnal mixing in the abyssal ocean. *Science* **264**: 1120–1123.
- , R. W. SCHMITT, K. L. POLZIN, AND E. KUNZE. 1997. Near-boundary mixing above the flanks of a midlatitude seamount. *J. Geophys. Res.* **102**: 947–959.
- VAN HAREN, H., N. OAKEY, AND C. GARRETT. 1994. Measurements of internal wave band eddy fluxes above a sloping bottom. *J. Mar. Res.* **52**: 909–946.
- WIEGAND, R. C., AND V. CHAMBERLAIN. 1987. Internal waves of the second vertical mode in a stratified lake. *Limnol. Oceanogr.* **32**: 29–42.
- WÜEST, A., D. C. VAN SENDEN, J. IMBERGER, G. PIEPKE, AND M. GLOOR. 1996. Diapycnal diffusivity measured by microstructure and tracer techniques. *Dyn. Atmos. Oceans* **24**: 27–39.

Received: 28 July 1997

Accepted: 21 July 1998

Amended: 15 January 1999